2022

Investigating the effect of CMAS Infiltration on Residual Stress of High Temperature Ceramic Coatings for Turbine Engines using 3D Confocal Raman Spectroscopy

Zachary Stein
University of Central Florida

INVESTIGATING THE EFFECT OF CMAS INFILTRATION ON RESIDUAL STRESS OF HIGH TEMPERATURE CERAMIC COATINGS FOR TURBINE ENGINES USING 3D CONFOCAL RAMAN SPECTROSCOPY

by

ZACHARY STEIN
B.S. University of Central Florida, 2020

A thesis submitted in partial fulfillment of the requirements
for the degree of Master of Science
in the Department of Mechanical and Aerospace Engineering
in the College of Engineering and Computer Science
at the University of Central Florida
Orlando, Florida

Fall Term
2022

Major Professor: Seetha Raghavan

ABSTRACT

Calcium-magnesium-aluminosilicates (CMAS), such as sand or volcanic ash, are ingested by aircraft jet engines during operation. CMAS then becomes molten while traveling through the combustor of the engine before depositing onto turbine blades within the turbine section of the engine. The molten CMAS melt infiltrates and interacts with the high temperature ceramic coated turbine blades. This infiltration increases coating stiffness and promotes coating phase destabilization, encouraging micro-crack formation and increasing the risk of spallation. Thermomechanical effects from CMAS infiltration were mapped over time with confocal Raman spectroscopy. The residual stresses within infiltrated 7YSZ EB-PVD coatings were captured with microscale resolution. The results show an interplay between both the thermomechanical and thermochemical effects influencing the residual stress state of the coating. Thermomechanical mechanisms have a prominent role on the residual stress early on in a coating's CMAS exposure and after 1 h of infiltration, inducing tensile stresses within the coating up to 100 MPa on tetragonal ZrO_2 Raman bands. Chemical mechanisms impart a greater influence on a much slower scale and after 10 h of infiltration, inducing compressive stresses within the coating up to 100 MPa. A monoclinic phase volume fraction of about 35% was observed to be a transitional point for thermochemical mechanisms overtaking thermomechanical mechanisms in dominating the residual stress of the coating. These results elucidate, in a non-destructive and non-invasive manner, changes within a coating's

residual stress as a result of CMAS exposure and the subsequent CMAS infiltration over varying annealing times. The results aid in the efforts to monitor coating degradation during maintenance and towards implementing CMAS-mitigation strategies in not only 7YSZ EB-PVD coatings, but also as a reference for more novel coating compositions under development.

I would like to dedicate this thesis work to my family for their continuous support and strength they give me to push through any difficulties and obstacles that I have faced along the way. To my research colleagues for providing me with the motivation to strive to constantly be a better researcher and team member as well as to constantly renew my excitement in my work, and finally to my advisor, Dr. Seetha Raghavan, for providing me with the opportunities to fuel my ambitions to achieve, succeed, and excel beyond any perceivable limits I ever had in my work so that I may accomplish and make possible the seemingly impossible.

ACKNOWLEDGMENTS

I would like to acknowledge Dr. Laurene Tetard & Chance Barrett for sharing the dataset for further analysis and access to Dr. Tetard's facilities. Dr. Ravisankar Naraparaju and Dr. Uwe Schulz at the German Aerospace Center in Cologne, Germany for the manufacturing of the samples within this thesis and for their support and guidance as advisors during my Fulbright Grant. I would also like to acknowledge the Fulbright U.S. Student Program and their Fulbright Academic Grant as well as the National Defense Science and Engineering Graduate (NDSEG) Fellowship Program for supporting me throughout my graduate studies and for the opportunities they gave me to expand, enhance, and elevate my work. Funding: This material is based upon work supported by National Science Foundation grants DMR 1337758, OISE 1460045, OISE 1952523, Fulbright Academic Grant, and the Department of Defense (DoD) through the National Defense Science Engineering Graduate (NDSEG) Fellowship Program and by the German Aerospace Center (DLR).

TABLE OF CONTENTS

LIST OF FIGURES

LIST OF TABLES

CHAPTER 1
INTRODUCTION

This chapter provides a background introduction on thermal barrier coatings, which includes their application in turbine engines, required to understand the problem with calcium-magnesium-aluminosilicates (CMAS), such as sand or volcanic ash. The second section of this chapter provides the motivation and organization of the thesis.

1.1 Thermal Barrier Coatings

Thermal barrier coatings (TBCs) are multi-layer coatings applied to the combustor and turbine engine components within gas turbine engines used in aeroengines and power generation to insulate these components from the hot gas streams of the engine. TBCs are applied to superalloy metallic components, such as turbine blades within the turbine section of the engine [1, 2]. TBCs reduce the surface temperatures of the superalloy turbine blades by approximately 200 °C due to the low thermal conductivity of a high temperature ceramic layer when also coupled with additional cooling methods, such as film cooling, to greatly improve the overall performance of aeroengines by allowing for higher operating temperatures as well as more durable engine components by extending its part lifetimes [3]. Currently, the two major industry standards for applying TBCs onto the

superalloy components are air plasma sprayed (APS) and physical vapor deposition (PVD), more specifically electron beam physical vapor deposition (EB-PVD). Each deposition method has its own benefits and applications. APS is generally more economical as compared to PVD methods and provides a dense, porous splat-like coating microstructure [2, 3]. APS coatings are prevalent within the power generation industry; however, these coatings can also be found within the combustor section and non-moving components held for long thermal cycles. EB-PVD, while more costly than APS, produces a closed porosity, columnar microstructure and provides higher in-plane strain tolerance and lower thermal conductivity in high-stress applications [3]. These characteristics are favorable to allow for thin coatings to operate under extreme environments in the turbine section with rotating turbine blades and frequent and short thermal cycling within aeroengines introducing additional external stresses onto the coating and their underlying components [2, 4]. TBC systems typically consist of four layers: a high temperature ceramic coating layer, a thermally grown oxide layer that forms throughout the lifetime of the TBC through interdiffusion of aluminum and oxygen, the bond coating adhering the ceramic coating to the metallic component, and the metallic superalloy substrate of the underlying turbine engine component. Each of these four layers serve a different function in order to increase the durability and lifetime of the underlying component [2, 5]. The thickness of the ceramic coating can vary from 150 – 400 μm depending on the deposition method and the desired temperature gradient from the hot gas stream to the surface of the substrate [2, 4]. The ceramic coating material has traditionally consisted of some weight variation of yttria with the zirconia polymorph, known as yttria-stabilized zirconia (YSZ) due to the low thermal conductivity of the tetragonal and cubic phases of zirconia. Previous

work has determined that 6 – 8 wt.% yttria provides the optimal lifetime of the TBC with 7 wt.% yttria being the industry standard (7YSZ) for YSZ coatings [1, 2]. An oxidation-resistant metallic bond coat (MCrAlY or PtNiAl) layer adheres the ceramic coating to the superalloy metallic substrate. During operation, oxygen diffuses inward towards the bond coat from the surface of the ceramic coating, bonds to the aluminum found within the bond coat, and forms a thermally grown oxide layer (TGO) of θ-Al_2O_3 that eventually turns into primarily α-Al_2O_3 between the bond coat and ceramic coating [6]. As the TGO layer grows, it restricts further oxygen diffusion between the ceramic coating and bond coat and therefore limits further growth over time [4, 7]. The α-Al2O3 is more compatible with the YSZ layer as compared to the metallic bond coat and substrate and helps to ensure long-term thermodynamic stability of the TBC system [8]. Finally, the nickel or cobalt based superalloy substrate is the gas turbine component that is to be insulated with the ceramic coating. The substrate is force air-cooled through internal cooling channels in order to establish a thermal gradient across the component and to better control the residual stress required for an optimal lifetime of the ceramic coating [4, 9].

1.2 Introduction to CMAS

Calcium-magnesium-aluminosilicates (CMAS) are chemical compositions that represent minerals typical of sand or volcanic ash. It is unavoidable during operation for aircraft engines to be exposed to CMAS in varying concentrations. Filters can be fitted to engines, such as inlet/inertial particulate separators, or cyclonic air filters applied to helicopter to reduce the amount of CMAS that comes

into contact with the engine, but these filters cannot prevent finer particle sizes, typically less than 100µm, from passing through these filters without further reducing the capabilities of the engines due to losses in the inlet pressure and mass flow [10, 11, 12]. Fig. 1.1 displays a global map of the fine particulate matter less than 2.5 microns in diameter ($PM_{2.5}$) concentrations estimates between 1998 - 2018 [13]. This $PM_{2.5}$ estimate between 1998 - 2018 displays the concentrations across the globe and while sand and volcanic ash are included within these measurements, it should also be noted that pollutants and other foreign object debris (FOD) are also included within these measurements and also influence the overall performance of an aircraft engine negatively.

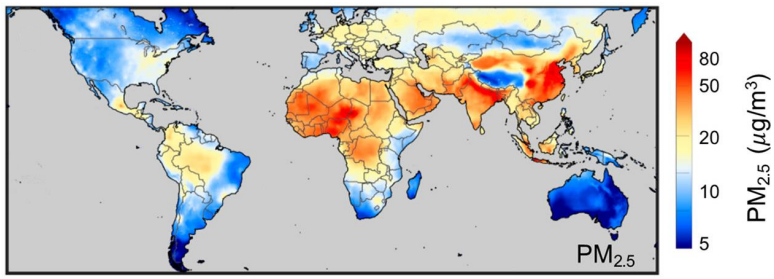

Figure 1.1: The outdoor particulate matter less than 2.5 microns in diameter ($PM_{2.5}$) concentration estimates between 1998-2018 on a global map [13].

The CMAS that is ingested into the engine will undergo one of two distinct forms of damage to the engine. The first is at lower combustion operating temperatures in which the combustor temperatures are below the CMAS melting temperature. The specific melting temperature will vary depending on the composition of the CMAS, but typically start between 1150 - 1300°C [14]. At these temperatures lower than melting, the CMAS particulates will travel along the free hot gas stream of the engine and eventually impact onto the moving turbine blade components or the walls

of the engine itself. These will cause erosion and impact damage to the coating. Over time, this impingement causes a loss in the volume of the coating as it is eroded away, reducing the overall effectiveness of the coating [15, 16].

The second form of damage is a form of corrosion. This damage occurs when the operating temperature is at or exceeds the temperature at which CMAS begins to melt. This form of corrosion attack will be the primary focus of this thesis and further outlined in the subsequent chapters. The CMAS particulates enter into the combustor and due to the extreme temperatures, becomes molten. In this molten state, the CMAS follows along the free hot gas stream as before and impinges onto a TBC coated surface. The molten CMAS melt then begins to wet the coating and starts to interact with it. The type and the extent of these interactions will depend on the ceramic coating's microstructure. For APS coatings, the CMAS melt will primarily rest on the surface of the coating and will only be able to further infiltrate into the coating through slower "wetting" of the coating or through any cracks or pores that might be present [17, 18]. For EB-PVD coatings, the CMAS melt will start to infiltrate between the columns through the intercolumnar gaps of the coating due to capillary effects and wetting the columns as it infiltrates further into the depth of the coating and starts to cool on contact with the coating [19]. Due to the thermal gradient present through the thickness of the coating, there will be some depth at which the CMAS will begin to solidify. A schematic illustrating the effects of CMAS-infiltration on 7YSZ EB-PVD coatings is provided in Fig. 1.2.

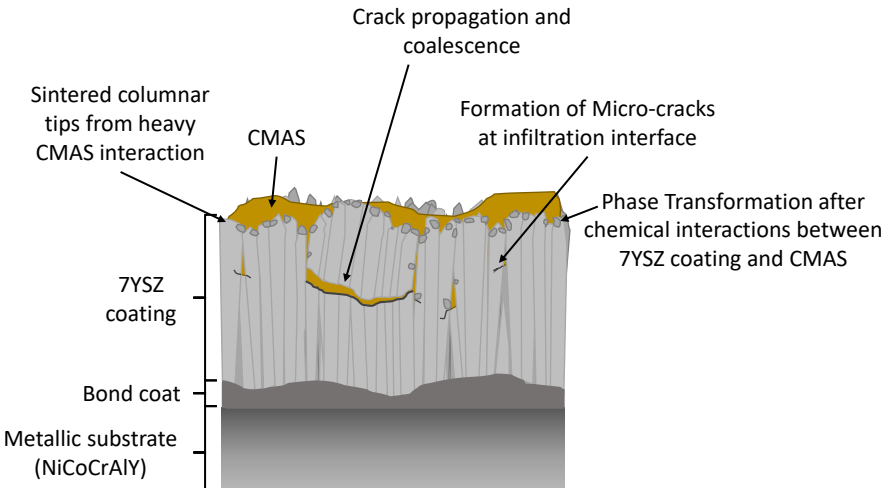

Figure 1.2: Schematic of a CMAS-infiltrated 7YSZ EB-PVD TBC system. The 7YSZ topcoat is infiltrated by CMAS. These effects of this infiltration includes the sintering of columnar tips and of the feather arms, micro-crack formation, propagation, and coalescence until causing localized coating spallation, and the localized formation of freely transformable ZrO_2 from the 7YSZ top coat. [20].

Upon solidification, either by reaching a certain depth through the coating's thermal gradient, or upon cooling during the thermal operational cycle, the CMAS will stiffen the EB-PVD columns and induce additional thermal stresses due to the coefficient of thermal expansion mismatch between the the CMAS glass and coating. The stiffened columns are fixed together, acting as a pseudo-bulk microstructure and can no longer freely expand and contract as required during thermal and mechanical loading from the engine operational cycle [21, 22, 23, 24]. These resulting additional stresses can be categorized as thermomechanical stresses. If these stresses are high enough, the coating may start to form microcracks and begin to locally fail through spallation

failure. This failure risk is a lot more likely if the CMAS infiltrates to some critical depth of the coating, which in practice tends to be around 50 - 60% of the coating thickness [25, 26]. Another category of stresses that form during CMAS attack onto high temperature ceramic coatings are thermochemical stresses.

Thermochemical stresses occur on a much slower time scale as compared to the thermomechanical stresses. These thermochemical stresses involve the interactions between the CMAS melt and the TBC system. While in its molten state, any part of the coating that comes into contact or is affected by the CMAS melt is commonly referred to as "wetted". Upon contact, the yttria (Y_2O_3) and zirconia (ZrO_2) begin to be leeched out into the CMAS melt. The zirconia quickly saturates within the CMAS melt as compared to the yttria and as a result, sintering occurs with the yttria-lean zirconia remaining in the CMAS-exposed coating [19, 22, 27]. With the yttria that once stabilized the zirconia into a tetragonal phase no longer being present, the zirconia polymorph is able to freely transform between different phases during an operational cycle. Of these different phases, the monoclinic phase, which forms at temperatures below around 600°C, is the most destructive due to a volumetric expansion of about 3 - 5% in the lattice structure between the tetragonal and monoclinic phases of zirconia [19, 21, 23, 25, 28, 29, 30, 31]. Additionally, Wellman et al., had found there needs to be some concentration of CMAS, 4.8 mg/cm^2 for their CMAS composition, required for thermochemical degradation to initiate on an observable level [32]. It is primarily this volumetric expansion that occurs within the coating that causes observable increases in the residual stress concentrations in which microcracks may start to form and cause localized coating failure.

Together, the thermomechanical and thermochemical components of this degradation introduces stresses, over time and in strong enough concentrations, will lead to premature coating failure. The extent of this failure will depend on how much the CMAS has infiltrated into the coating as well as to what extent the CMAS has interacted with the coating over time. Regardless, this premature coating failure is an inherent risk that needs to be mitigated to the point where engine components do not unexpectedly fail during operation and cause catastrophic total engine failure with metallic components experiencing higher and unsafe temperatures during operation.

1.3 Techniques for non-destructive detection (Raman Spectroscopy)

Techniques and methods can be utilized to measure and monitor the effects of CMAS on the TBCs within the engine. The aircraft industry already have both destructive and non-destructive measurement techniques they employ during routine aircraft inspection. In high CMAS-abundant regions, these inspections occur on a much regular basis due to the more extreme and harsh operational environment the aircraft are expected to function under. Internal surface visual inspections are performed through a borescope to check for the evidence of CMAS caking and build up and are easily implemented for inspecting CMAS-related exposure [11, 33]. Additional methods involve removing the airfoil turbine blade from the engine entirely and performing a series of destructive and non-destructive measurements. Raman Spectroscopy has been used in this thesis with the idea in mind of being a potential technique for routine aircraft inspection. Raman spectroscopy, first discovered and developed by C.V. Raman, uses optical excitation to excites the phonon or vibra-

tional bonds of the lattice structure of a material, providing a spectra from the changes in energy. This spectral signal, coming from Stokes and anti-Stokes scattering, albeit weaker than Rayleigh scattering, is unique to the probed phase composition and provides additional information such as the stress distribution, vacancies or other changes within the lattice structure. As such, Raman Spectroscopy is ideal to track the thermochemical changes from CMAS-exposure through capturing the phase concentrations, phase volume fraction, due to phase transformations occurring within the coating [27]. Thermomechanical changes from CMAS-exposure can be captured to monitor changes within the residual stress state of the coating over time. These thermomechanical changes have yet to be fully quantitatively captured with high spatial resolution on a microscale while also capturing pristine subsurface measurements unaffected by post-manufacturing/processing related stress relief, which is the focus in this thesis.

1.4 Motivation

CMAS exposure on TBCs and the subsequent interaction of CMAS with the coating causes premature failure. The failure of these coatings compromises the overall TBC system as well as present a potential risk of component failure since the underlying metallic component is now exposed to higher than nominal temperatures during operation. This puts the entire engine at risk for catastrophic failure. It is therefore vital to capture both the thermochemical as well as the thermomechanical effects of CMAS exposure on these high temperature ceramic coatings and to be able to quantify these degradation mechanisms from CMAS infiltration to better elucidate the

potential critical point of failure of coatings and the subsequent effects of this failure to the overall TBC system itself. This is achieved within this thesis through 3D confocal Raman Spectroscopy. Better understanding the interdependent relationship between these thermomechanical and thermochemical infiltration kinetic micro-mechanisms aids in the design, development, monitoring, and assessment of mitigation strategies for novel coatings to promote longevity in CMAS-exposed coatings.

1.5 Overview of Thesis

The content of this thesis is divided into chapters organized in the manner that goes into depth each component required to better understand and supports the aforementioned motivation. The chapters are arranged as follows:

Chapter 2 provides a more in-depth introduction CMAS, giving the history of the CMAS problem with high temperature ceramic coatings, discussing more on the infiltration kinetics for 7YSZ EB-PVD coatings, as well as the development of CMAS-related studies on a laboratory scale.

Chapter 3 discusses more on the theory of Raman spectroscopy and how Raman spectroscopy has been used in literature on studying ceramic coatings and CMAS infiltration.

Chapter 4 dives deeper into the manufacturing process of the samples and CMAS composition used within this thesis as well as discussing previous Raman Spectroscopy work led by Barrett et al., [27], focusing on the quantification of the thermochemical degradation of CMAS-infiltrated 7YSZ EB-PVD coatings tracked through the monoclinic phase volume fraction over increased

annealing times.

Chapter 5 investigates the thermomechanical components of the CMAS infiltration kinetics through quantifying and tracking the changes in the residual stress states of CMAS-infiltrated 7YSZ EB-PVD coatings over increasing annealing times. These are the main findings presented within this thesis and have also been published [20].

Chapter 6 provides a summary of the conclusions from the thesis in a manner that highlights the impact of this thesis. A future work and plans of the scope in potential future studies are also provided that build upon the work of this thesis.

CHAPTER 2
THEORY OF CMAS AND CMAS-INFILTRATION INTO THERMAL BARRIER COATINGS

This chapter provides an introduction to calcium-magnesium-alumiosilicates (CMAS), such as sand or volcanic ash. The first section in this chapter provides a short history of CMAS and the issues it caused to helicopters and aircrafts operating within regions such as the Middle East. The section of this chapter also provides the theory regarding CMAS infiltration kinetics and how it affects thermal barrier coatings as well as other high temperature ceramic coatings. Additionally this chapter talks about the thermomechanical and thermochemical mechanisms that dominate the interactions between CMAS and thermal barrier coatings. Thermomechanical mechanisms occur instantly as the CMAS infiltrates and begins to solidify within the coating, stiffening the columnar microstructure of the electron-beam physical vapor deposited (EB-PVD) coating and allowing for microcracks to form due to coefficient of thermal expansion mismatch between the coating and solidified CMAS as well as at the interface between the CMAS-infiltrated and non-infiltrated regions of the coating. Thermochemical mechanisms occur over a longer timeframe, primarily through coating destabilization as CMAS interacts and leeches out Y_2O_3 and a minor amount of ZrO_2 from the 7YSZ thermal barrier coating. Without the Y_2O_3 stabilizing the ZrO_2 polymorph, locking it within a tetragonal phase (known as tetragonal-prime), the yttria-lean ZrO_2 is able

to freely transform into the cubic and monoclinic phase; the latter which involves a volumetric expansion and further promotes microcracks to form within the coating. Finally the third section of this chapter discusses the synthesis of various CMAS compositions for laboratory usage and the application of this simulant for laboratory-scale research.

2.1 High Temperature Ceramic Coatings

Metallic alloy components, such as turbine blades within gas turbine jet engines, operate in extreme conditions and are usually protected by high temperature ceramic layers referred to as thermal barrier coatings (TBCs). These high temperature coatings provide a temperature gradient of approximately 150 - 200°C with respect to the hot environment [3]. TBCs and additional cooling methods, such as film cooling, are used to increase the temperature gradient from the hot gases produced by the combustion section of the engine in the effort to further improve the performance, durability, and to extend the life of the hot section components [2, 5, 34, 35]. A TBC system comprises of several layers including a ceramic top coating, a thermally grown oxide layer (TGO) that forms throughout the life cycle of the coating, and a metallic bond coat used to better the adhesion between the ceramic coating and underlying metallic superalloy component [4]. During operation, oxygen diffuses into the TBC system from the surrounding free hot gas stream environment and aluminum diffuses upwards from the bond coat to meet with the oxygen. Typically α-Al_2O_3 forms at these high operating temperatures once the aluminum and oxygen meets, forming the TGO layer. Further oxidation is inhibited as the TGO layer grows during the lifetime of the TBC

[36]. An industry standard material used for the ceramic top coats is 7 wt.% yttria partially stabilized zirconia (7YSZ), corresponding to approximately 4 mol% Y_2O_3-ZrO_2, due to its low thermal conductivity and high mechanical strength [2, 37]. Several methods can be used when depositing TBCs, such as air plasma spray (APS) and electron-beam physical vapor deposition (EB-PVD). EB-PVD, the deposition method used to produce the samples within this thesis, produces characteristic closed-porosity columnar structures, which provide high in-plane strain tolerance, lower thermal conductivity, and excellent thermal shock protection. These attributes are ideal for moving components, such as turbine blades [19, 38]. However, 7YSZ coatings are susceptible to severe mechanical and chemical degradation, which can catastrophically endanger the functionality of hot section components as well as the engine itself, when operating in harsh environments. Exposure to contaminants from the external environment of the engine can have detrimental effects on the effectiveness and operational lifetime of TBCs [21, 30, 39, 40, 41].

2.2 History of CMAS

During operation, jet engines are subjected to a variety of external environmental conditions that can translate into airborne contaminants being ingested by the engine. Such contaminants are calcium, magnesium and alumino-silicates (CMAS) dominated compositions, such as sand or volcanic ash. CMAS is ingested into the engine and may become molten due to the high temperatures of the combustor during operation. This molten CMAS melt is then carried to the turbine section of the engine and is then deposited onto the turbine blades. The molten CMAS rapidly infiltrates

into the coatings and fills the intercolumnar gaps of the top coat for EB-PVD coatings, such as 7YSZ, through strong capillary effects [19, 21, 40, 42, 43]. However, CMAS is not just an issue for aircraft engines, but also the turbine airfoils of helicopters.

In 1991, Smialek et al. had identified compositions and determined the effects in the build up of deposits on the leading-edge of vane platforms as well as the powdery substances within the cooling passages of the turbine disc for helicopters operating at low-altitudes in the Middle East during the Persian Gulf War. Smialek et al. found degradation of the airfoil to be from the high operating temperatures in the presence of CMAS silicate deposits as well as these deposits clogging the cooling holes [39]. This opened further investigations on the role of CMAS in both the cool and hot sections of turbine engines in power generation as well as in military and commercial aircraft operations [21, 44].

It was also observed that the compositions of the CMAS from the engine deposits tended to be significantly different from the common sources of CMAS from the surrounding environment, which was also reported by Smialek et al. and shown in Fig. 2.1. As a result, the literature reported widely varying chemical compositions of sand found both within the engines as well as the regions where these aircrafts operated [40]. Synthesized CMAS tried to replicate the compositions to mimic the infiltration conditions and effects found with the field studies in a laboratory setting [22, 26, 30, 44, 45]. Additionally, investigations focused on characterizing the effects of CMAS degradation on coatings at various experimental parameters, such as changing the calcia or silicate deposit concentrations and as well as replicating and modifying the environmental conditions within the engine.

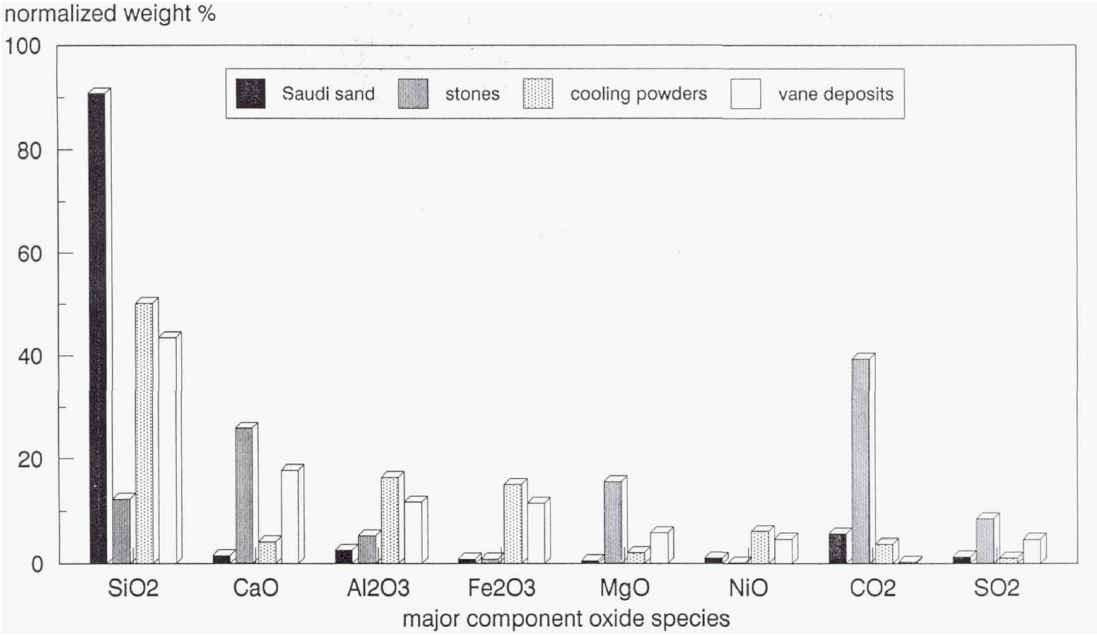

Figure 2.1: The major oxide species present, normalized by weight %, of Saudi Arabian sand, river bed stones, what was observed by Simalek et al. in the powders found in the cooling channels, and within the vane deposits [39].

2.3 CMAS infiltration kinetics

At temperatures lower than the melting range of CMAS, particle impact and erosion damage was determined to be a major contributor towards coating failure resulting from CMAS exposure [32, 45, 46]. Meanwhile, within and above the melting range, it was found that thermomechanical and thermochemical degradation played prominent roles in the degradation of TBCs. The exact melting range of CMAS depends on the chemical composition of the CMAS, but typically starts to

occur around 1200°C [40]. The work in this thesis will focus on infiltration temperatures within the melting range of CMAS due to the detrimental and complex degradation effects it has on coatings from infiltration during operation. A schematic by Evans et al. illustrates the effects of CMAS attack from impact and erosion damage to its infiltration effects in Fig. 2.2 as well as an image of a turbine blade exposed to CMAS demonstrating the real-world effects of CMAS-exposure [47].

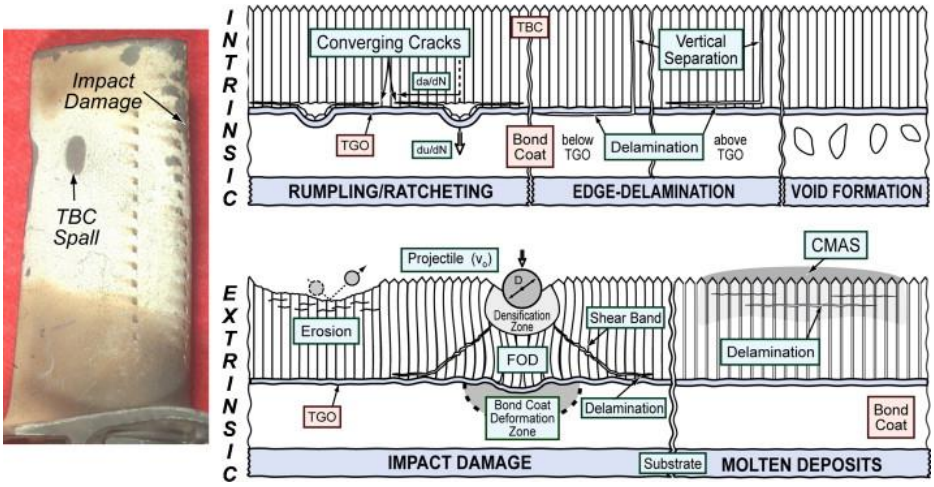

Figure 2.2: (Left) An image of a turbine blade exposed to CMAS and exhibiting both impact damage as well as coating spallation. (Right) Schematics showing the intrinsic and extrinsic influences on coating failure. Primarily focusing on the effects of CMAS below and at CMAS melting temperatures within the extrinsic factors schematic [47].

2.3.1 Thermomechanical mechanism kinetics

The depth at which CMAS infiltrates into the coating as well as the extent and rate of coating degradation is dependent on a variety of factors regarding the CMAS composition, its viscosity, the microstructure and material properties of the coating, the thermal gradient present throughout the coating, the ambient hot gas temperature, and environmental conditions such as humidity within the turbine section to name a few [19, 48]. Similarly, the existing literature has found a critical depth of infiltration, beyond which the coating is highly susceptible to delamination failure [25]. Experimentally, this critical depth of infiltration tends to occur around 50 - 60% infiltration [25, 30]. The CMAS melt begins to solidify within the coating as it infiltrates and reaches cooler temperatures below its melting point due to the temperature gradient present. The solidified CMAS effectively clogs the intercolumnar gaps, creating a pseudo-bulk CMAS glass and 7YSZ column structure and, as a result, stiffens the overall coating. This columnar stiffening decreases the strain tolerance, introduces mismatching coefficients of thermal expansion, and increases the overall thermal conductivity of the coating [23, 30, 49, 50]. The now sealed intercolumnar gaps are unable to provide relief from thermal expansion to the columns during cycling. If the CMAS has not fully infiltrated throughout the coating and its intercolumnar gaps before cooling, two distinct regions form through the depth of the coating [51]. The infiltrated region will experience additional tensile stresses with the increased stiffness and decreased coating porosity [21, 23, 24, 50]. This bulk region also induces bending forces onto the interface between the infiltrated and non-infiltrated regions. The resulting residual stresses present within the coating coupled with thermal loading

and coefficient of thermal expansion mismatches between these two regions of the coating during operation will cause microcracks to form and coalesce if the stresses introduced into the coating are severe enough. These microcracks will lead to localized delamination and eventual premature coating failure at this infiltrated and non-infiltrated interface [40, 50, 52]. Naraparaju et al. had tailored the microstructure of 7YSZ EB-PVD coatings by modifying the deposition parameters and found that extending the feather arms present on the sides of the EB-PVD columns slowed down the rate of infiltration [19]. At a higher viscosity, with the CMAS only partially melted, the CMAS only infiltrated to half the depth of conventional EB-PVD coatings. Similarly, at a lower viscosity, with the CMAS fully melted, the CMAS fully infiltrated the coating in about eight minutes as compared to full infiltration taking about five minutes for the control coating [19]. What this study demonstrates is that not only can the microstructure be modified to lower the infiltration rate with respect to a coating's depth, but also of how conditions, such as the operating temperature, can influence factors such as viscosity, which directly impacts how CMAS interacts and infiltrates into coatings.

2.3.2 Thermochemical mechanism kinetics

Additional chemically-induced stresses form within the coating as it interacts with the molten CMAS and the coating becomes destabilized. Primarily, yttria (Y_2O_3), used to stabilize the zirconia (ZrO_2), keeping it locked into the tetragonal phase, referred to as tetragonal-prime. When exposed to CMAS, the yttria is leeched from the coating into the CMAS melt over time. Small

amounts of the zirconia are also leeched into the CMAS. However, the zirconia quickly becomes saturated within the melt as compared to the yttria, allowing for more yttria to be removed from the coating as compared to the zirconia itself [22, 53, 54, 55]. This interaction between the CMAS melt and YSZ coating contributes to the sintering of columnar tips and feather arms on the edges of the columns. Without yttria to stablize the zirconia polymorph, the now yttria-lean coating can freely transform from its once stable yttria-rich coating in the tetragonal-prime phase to an yttria-lean tetragonal, cubic, or monoclinic phase[22, 32, 40, 50, 53]. Levi et al. produced a schematic demonstrating the chemical interactions of CMAS with 7YSZ EB-PVD coatings, as shown in Fig. 2.3 [40].

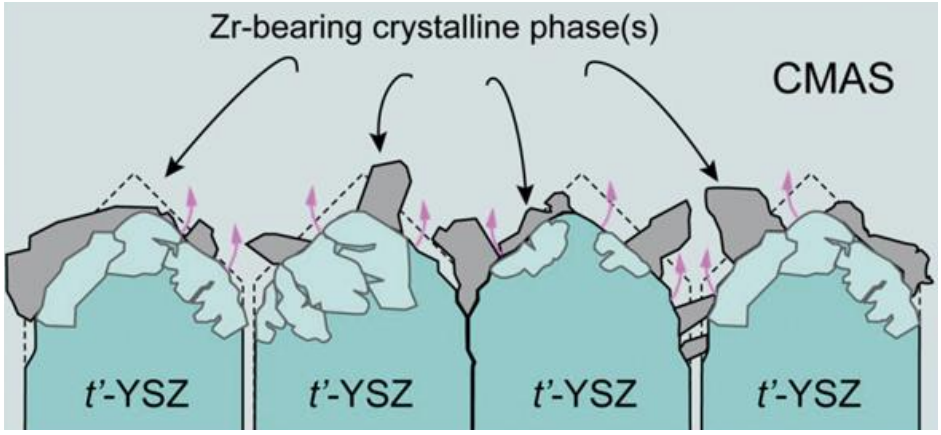

Figure 2.3: Schematic portraying the chemical interactions of CMAS with 7YSZ EB-PVD columns. Some of the coating is dissolved into the CMAS melt and eventually reprecipitates back, allowing for sintering to occur. Meanwhile, yttria is leeched from the non-dissolved coating, allowing for phase transformations to occur [40]

The monoclinic phase itself poses several problems with its associated volumetric increase in the lattice structure of about 3 - 5% as compared to the tetragonal phase [28, 29]. The monoclinic phase has been found to start forming around 600°C and lower [31]. This expansion introduces additional localized residual stresses, which contribute towards the premature failure of the coating [19, 21, 23, 25, 28, 29, 30, 50, 52, 56, 57]. This thermochemical mechanism of phase destabilization and transformation is delayed and much slower acting than the thermomechanical effects of CMAS infiltration through CMAS-induced coating stiffening [22, 26]. A schematic demonstrating the effects of CMAS infiltration into 7YSZ TBCs on the residual stress was displayed in Fig. 1.2. In this thesis, further elucidation will be performed regarding the residual stress evolution effects of CMAS infiltration into 7YSZ EB-PVD TBCs over time through a non-destructive confocal Raman spectroscopy technique [58, 59].

CHAPTER 3
RAMAN SPECTROSCOPY THEORY AND RELATED EXPERIMENTAL METHODS

This chapter first discusses Raman spectroscopy, how the laser excites the phonons and vibrational bonds between materials, and its nondestructive nature in characterizing materials through phase composition, stress, texturing, and disorder. The second section of this chapter discusses the previous literature of Raman spectroscopy with thermal barrier coatings both with and without CMAS infiltration. The third section of this chapter discusses a novel technique coupling confocal microscopy with Raman spectroscopy that provides a non-invasive and nondestructive of a way to probe 3D volumes of thermal barrier coatings from the surface of the coating and its ability to provide the typical Raman information with a microscale resolution within its spectra towards characterizing coating degradation over time.

3.1 Theory of Raman Spectroscopy

When a laser impinges onto a material, the energy from the laser excites the phonons, or the vibrational bonds, of the material composition. A vast majority of the incident energy impinging onto the material and its vibrational bonds is released in an elastic process, meaning at an equivalent

amount with no energy lost or gained overall in the return signal, also known as Rayleigh scattering. However, there is a very small amount, approximately 1×10^{-6} % of the light will undergo an inelastic process, meaning the light interacted with the molecular vibrations of the material. In this inelastic process, the emitted photons from the excitation may emit more energy compared to the incident photon, known as Anti-Stokes Raman scattering, or the emitted photons from the excitation may emit less energy compared to the incident photon, known as Stokes Raman scattering. A schematic by Cho and Ahn demonstrating the changes in photon excitement levels with respect to Rayleigh, Anti-Stokes Raman, and Stokes Raman scatterings is represented in Fig. 3.1. Generally, Stokes Raman scattering is used for measurement analysis since it is more sensitive as compared to Anti-Stokes Raman scattering.

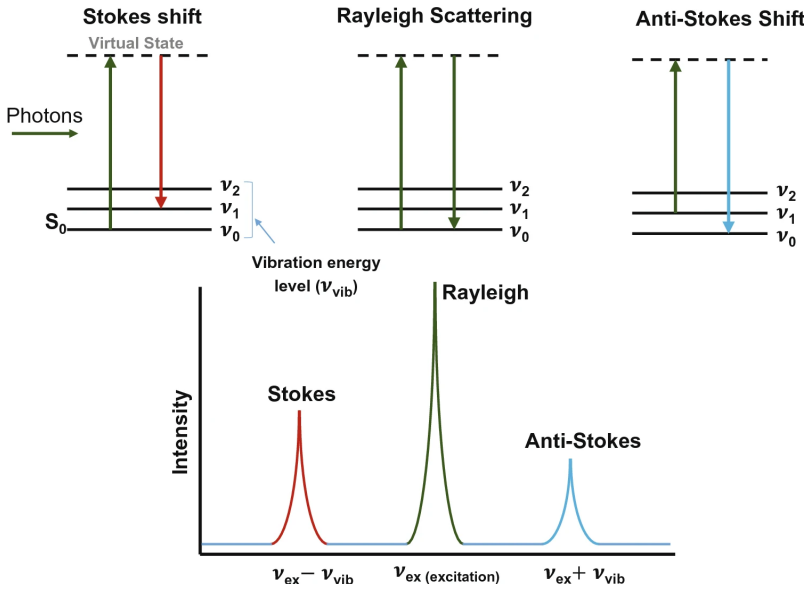

Figure 3.1: Schematic displaying differences in photon emission excitation levels involving Rayleight scattering as well as Stokes and Anti-Stokes Raman scattering and how these different scatterings appear when plotted by Intensity and Raman Shift (cm^{-1}) graphs [60].

This observation of inelastic scattered light was first noticed by Sir C.V. Raman and his student at the time, K.S. Krishnan in 1928 [61]. Since the inelastically scattered light interacts with the vibrational bonds of the impinged material, Raman scattering produces what is known as a Raman spectra, with the units of relative wavenumber or Raman Shift (cm^{-1}). This Raman spectra is unique towards the molecules and the overall material composition, meaning information regarding the probed material's composition and its phases can be determined through this technique of Raman Spectroscopy. Since the laser does not alter the molecules or vibrational bonds of the material in any destructive or irreversible way, outside of potential photobleaching effects on unstable fluorophores, Raman spectroscopy is considered to be a non-destructive technique.

When the vibrational bonds are stretched or compressed due to external forces, the resulting Raman spectra is also influenced. This is to say, when the probed material experiences tensile or compressive forces, the subsequent Raman spectra is affected through changes in the Raman shift, allowing to qualitatively measure internal and external stresses applied to the probed material. Fig. 3.2 shows the Raman spectra for nanometer-sized tetragonal zirconia grains applied under increasing hydrostatic pressure loadings up to 31 GPa measured by Bouvier and Lucazeau [62]. Shifts in the peak locations of this Raman spectra can be observed through the increasing pressure loads. These shifts can then be plotted with respect to the applied loading and peak location to obtain the pressure dependency of the Raman peaks. Under small loads, up to about 12 GPa in Fig. 3.2, a linear regression can be fitted to the peak location shifts.

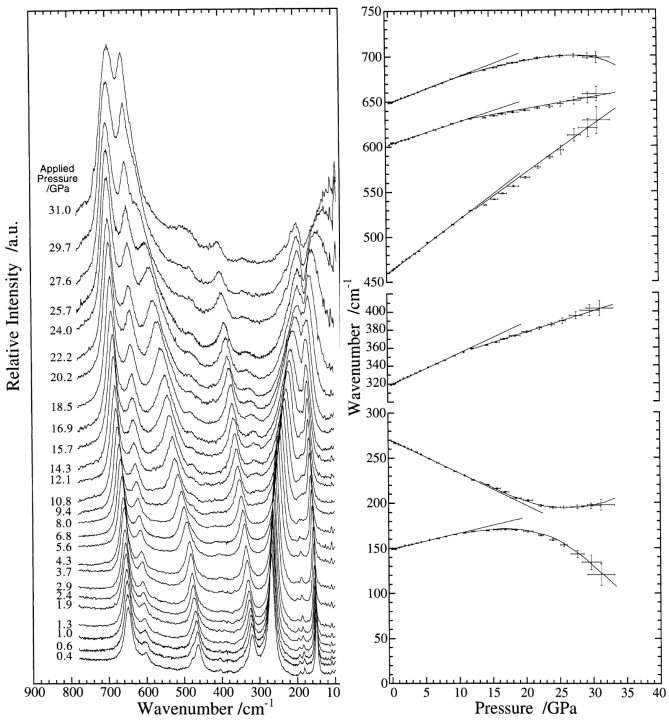

Figure 3.2: Modified figure from Bouvier and Lucazeau, *J Phys Chem Solids* (2000), where (left) the Raman spectra for nanometer-sized tetragonal zirconia grains under increasing hydrostatic loading up to 31 GPa and (right) the pressure dependence of the Raman peak locations for 150, 260, 320, 480, 602, and 650 cm^{-1} peaks along with their linear regressions used to determine their piezo-spectroscopic coefficient [62].

The resulting slope, along with the measured peak location, can be used on other Raman spectra of tetragonal zirconia to determine the loading or stress that the tetragonal zirconia is experiencing. This allows for the quantification of stress in the probed material, so long as it is below the aforementioned 12 GPa for the zirconia polymorph. This quantification of stress works for both internal residual stresses as well as externally applied stresses.

3.2 Brief Literature review of Raman Spectroscopy and 7YSZ EB-PVD TBCs

Due to the Raman spectra holding information regarding the phase volume fractions as well as stresses experienced by the probed material, Raman spectroscopy has been utilized over the past few decades to analyze thermal barrier coatings and different characteristics of these high temperature ceramic coatings. Typically these studies are coupled with additional measurement techniques, such as scanning electron microscopy (SEM), X-ray diffraction (XRD), and energy-dispersive X-ray spectroscopy (EDAX) to name a few. Some fundamental, yet essential, measurements regarding finding the piezo-spectroscopic coefficients for different coating compositions have been done, such as from Tanaka et al., who looked at a free standing 7YSZ EB-PVD coating [63]. Additional Raman measurements often consider phase evolution over time for 7YSZ, doped variants of 7YSZ, and of more novel coatings such as gadolinium zirconate ($Gd_2Zr_2O_7$) [27, 64, 65]. Measurements have also been taken to observe how changes in the peaks of Raman spectra occurs over time, such as sharpening or broadening [66]. A prominent measurement often taken is measuring the stress state of the coating under different deposition parameters and conditions, through doped coatings, or throughout cycling [67, 68, 69].

Similarly, Raman spectroscopy studies have been performed on CMAS exposed TBCs and the resulting effects of CMAS infiltration. These studies often looked at phase compositions as well as stress measurements just as their non-CMAS-infiltrated counterparts. Often for 7YSZ, the most observable changes in the phase evolution of CMAS-infiltrated coatings, is the formation of the monoclinic phase. This formation can be tracked as well as qualitatively seen to increase in

its concentration over time and throughout the depth [22, 23, 49, 52, 70, 71]. The effects of the chemical composition of CMAS has on the ceramic coating has also been studied. Ultimately, it was found that the calcia and silica ratios (CaO/SiO_2) plays a big role on how aggressive the CMAS reacts with the 7YSZ coating and the mechanisms that dominate the the CMAS-7YSZ reaction [**?**]. Minor constituent species within the CMAS mixture, such as titanium dioxide (TiO_2) and iron oxide (FeO), can influence the resultant species products that form when the CMAS melt interacts with the coating, increasing the chances of forming zirconolite, fluorite, garnet and apatite compositions [55].

In-situ Raman measurements have been taken regarding the formation of different zirconia phase peaks after CMAS exposure throughout different temperatures [31]. It should be noted that in-situ experiments at high temperatures has its own considerations, such as peak widening with increasing temperatures, that must be taken into account. CMAS has also been observed to induce tension within the residual stress measurements [50]

3.3 3D Confocal Raman Spectroscopy

Higher spatial resolutions are achieved when coupling microscopy with Raman spectroscopy to focus the laser. A focal point is created when redirecting the laser through some objective lens, outside of which, the laser is considered to be unfocused. An Airy disk superimposing the focused and out-of-focus regions of data collected forms as a result [72, 73]. The diameter of the Airy

disk can be approximated with eq. 3.1, where λ is the excitation wavelength, *NA* is the numerical aperture, and *n* is the refractive index.

$$R_{Lateral} = \frac{1.22n\lambda}{NA} \tag{3.1}$$

It should be noted that the shape of the laser and its probed volume is conical in nature and has the cross-section of an airy disk when observing along the incident laser plane. An example of this conical shape is shown with varying numerical apertures in Fig. 3.3.

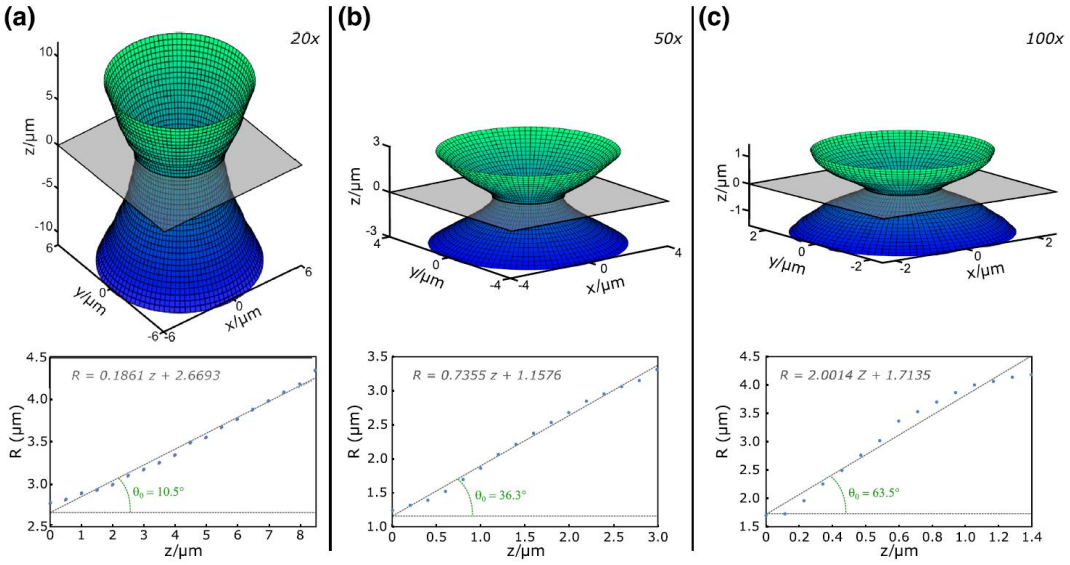

Figure 3.3: The shape of the laser beam at the surface of a probed silicon sample for (a) 20x, (b) 50x, and (c) 100x objective lens and the subsequent laser radius with respect to the distance from the surface of a silicon sample [72].

This boundary between the focus and out-of-focus regions will depend on various instrumental parameters, such as the aperture distance and the numerical aperture of the lens. The smaller the

aperture distance, the more out-of-focus signal will be blocked, but at the expense of reducing the return beam output to the CCD. The higher the numerical aperture of the lens is, the smaller the working distance is, the higher the spatial lateral resolution will be, as described theoretically in eq. 3.2, and the higher the depth resolution will be, as described theoretically in eq. 3.3, where λ is the excitation wavelength, *NA* is the numerical aperture, and *n* is the refractive index.

$$R_{Lateral} = \frac{0.61n\lambda}{NA} \tag{3.2}$$

$$R_{Depth} = \frac{2n\lambda}{NA^2} \tag{3.3}$$

Taking both the lateral and depth spatial resolutions in mind, the focal point can be moved to create a planar map across the same depth into the coating (lateral) or focused deeper into the coating (depth). Taking a 2D map across the same focal depth before changing the focal point deeper into the coating to take another 2D map across the new focal depth and repeating this process allows for the creation of a 3D probed volume of Raman data. It should also be noted that the refractive index will change going into the coating as compared to the laser traveling only through air to reach the surface of the coating. The refractive index will vary depending on the coating's microstructure, but tends to be around 1.6 for pure CMAS and 2.19 for pure zirconia compositions, separately [74]. Another thing to consider is more and more focused signal will be "lost" as the focal point shifts deeper into the coating since the laser will need to traverse through more and more material to reach the desired focal point. This will result in a higher out-of-focus information being collected and signal intensities decreasing over increasing depths. Therefore, a

microstructure that is more porous or has intercolumnar gaps of air, such as with EB-PVD, while making the changing probed volume more complicated at higher spatial resolutions, also allows for more in-focus data since the laser is unhindered for much further into the depth of the coating if probing the edge of a column as compared to a bulk splat-like monolithic microstructure. With these considerations in mind, 3D confocal Raman Spectroscopy is possible and produces these 3D probed volumes for data analysis where each point within the volume contains a Raman spectra for the probed region, whose size is defined by the lateral and depth resolutions. This novel technique was first published in previous work, which is discussed more in Chapter 4.2.2 as well as in patents [58, 59] and has been used within this thesis and its corresponding journal publication [20].

CHAPTER 4
MANUFACTURING AND PROPERTIES OF CMAS-INFILTRATED TBCS

Contents within this chapter have been published in:

C. Barrett, Z. Stein, J. Hernandez, R. Naraparaju, U. Schulz, L. Tetard, and S. Raghavan, "Detrimental effects of sand ingression in jet engine ceramic coatings captured with Raman-based 3D rendering." *Journal of the European Ceramic Society*, vol. 41, no. 2, pp. 1664-1671, 2021. doi: 10.1016/j.jeurceramsoc.2020.09.050 [27]

This chapter outlines the manufacturing processes used to synthesize and apply the calcium-magneisum-aluminosilicate (CMAS) paste to 7YSZ EB PVD samples used within this thesis. Prior efforts are also discussed including a cross-sectional validation of the 3D confocal Raman measurements as well as quantifying the chemical degradation tracked through the monoclinic phase volume fraction concentrations within the measured probed volume, providing a thermochemical analysis of CMAS-infiltration within the later sections of the chapter.

4.1 Manufacturing and Processing of CMAS-Infiltrated 7YSZ EB-PVD Samples

A 150 kW electron-beam physical vapor deposition (EB-PVD) system at the German Aerospace Center (DLR) in Cologne, Germany was used to produce 400 μm 7YSZ coatings deposited onto alumina substrates. These coatings were produced with higher thicknesses than average to isolate and study the CMAS infiltration kinetic effects in the EB-PVD coatings. The potential effects from the substrate are minimized with a control sample annealed without any CMAS infiltration. This not only provides a baseline, but also isolates any thermochemical and thermomechanical effects induced solely by CMAS infiltration. During the deposition process, the alumina substrates used were placed on a sample holder with a rotational speed of 12 rpm directly above the YSZ ingot with a substrate temperature of 1000°C. More information regarding the sample fabrication and manufacturing can be found in [27].

4.1.1 CMAS composition and fabrication

The CMAS composition was derived from compositions found within aero-engines operating within Middle Eastern countries (in mol.%: 24.6% CaO, 12.4% MgO, 11% Al_2O_3, 41.7% SiO_2, 8.7% FeO & 1.6% TiO_2) as previously described in [19, 27]. The CMAS powders were artificially synthesized through the co-decomposition of SiO_2 and TiO_2 as well as Me-nitrates powders. The process of this producing these CMAS powders are described in greater details in [19].

4.1.2 CMAS infiltrated TBC preparation

A paste of CMAS in a concentration of 10 mg/cm^2 was applied on the 7YSZ coating and infiltration experiments were performed at an annealing temperature of 1250°C. A 10 K/min heating and cooling rate in a laboratory box furnace was used. Two annealing times of 1 h and 10 h were selected to understand short-term and long-term infiltration kinetic effects of molten CMAS in 7YSZ coatings. This provides initial observations on the time dependency effects of CMAS infiltration with respect to coating stress evolution, of which can be further expanded upon in the future with full coating systems and with higher temporal resolutions.

A summary of the samples within this thesis is provided in Table 4.1. A control sample composed purely of 7YSZ without any CMAS infiltration (A3) was used as a reference to rule out the effect of high temperature annealing on 7YSZ and to serve as a reference coating state. Any variation from this reference would then demonstrate the resulting effects of CMAS infiltrated in 7YSZ for the chosen 1 h (B2) and 10 h (B3) annealing times. Validation was performed on a cross section of a CMAS infiltrated TBC annealed for 10 h (B3). More information on the validation measurements carried out on this cross-sectioned sample to the probed volume with the confocal non-destructive approach used within this thesis can be found in Chapter 4.2.1 and in [27].

Table 4.1: Samples information regarding composition, annealing temperature, and annealing time.

Sample	Composition	Temperature (°C)	Time (h)
A3	7YSZ	1250	10
B2	7YSZ + CMAS	1250	1
B3	7YSZ + CMAS	1250	10

4.2 Experimental Efforts of CMAS-Infiltrated 7YSZ EB-PVD Coatings

The Raman spectroscopy measurements were performed on an Alpha 300RA WITec Confocal Raman microscope equipped with a He:Ne 532 nm laser source excitation. A 20X objective lens was used for data collection. The 20x objective lens has a numerical aperture of 0.4, which corresponds to a Z-resolution of 6.65 μm and XY-resolution of 0.8 μm. An excitation laser power of 11 mW and additional collection parameters, including an integration time of 20 s, remained constant for all the data reported in this study. The Rayleigh scattering was filtered with a notch filter and the inelastically scattered light was split with an 1800 g/mm grating. A step size of 1 μm was used for the line scans and 2D maps as to prevent potential overlapping of probed points from the theoretical 0.8 μm lateral resolution. Each 2D map consists of an array of 20 × 20 spectra, corresponding to 400 spectra being collected for a total acquisition time of 8000 s. The detection spectral range covered during these measurements range between 100–800 cm^{-1}. 2D Raman spectral maps at increasing depths were collected by focusing the light at increasing positions beneath the surface to assess CMAS degradation by the corresponding localized residual stress changes in

7YSZ. The step size between these different depth planes was 6.65 μm, which corresponds to the axial resolution limit for the 20x objective lens used within this study.

4.2.1 Cross-Sectional Validation of 3D Confocal Raman Measurements

A brief description of what 3D confocal Raman spectroscopy was mentioned in Chapter 3.3. This novel method was validated by taking cross-sectional data through the coating's thickness to a size that matched the probed volumes between the two methods of data acquisition and the two results were compared, as shown in Fig. 4.1 [27].

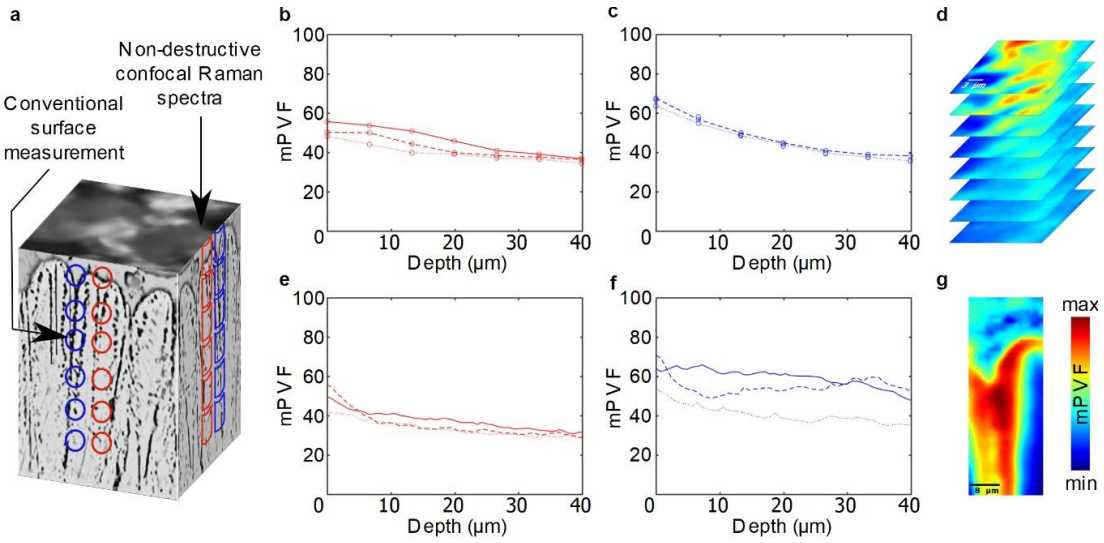

Figure 4.1: Comparison of 3D confocal Raman spectroscopy and cross-section Raman spectroscopy. (a) Representation (not to scale) of a 3D volume of CMAS infiltrated EB-PVD 7YSZ used for validation of the 3D confocal Raman spectroscopy approach for non-destructive analysis. The rectangles represent the edge (blue) and center (red) of the column as a depth measurement taken with 3D confocal Raman spectroscopy. The circles represent the cross-sectional surface measurements. (b-d) mPVF measured through confocal Raman spectroscopy at (b) the center, and (c) the perimeter of column. (d) Successive 2D maps of mPVF obtained. Scale bar indicates 3m. (e-g) mPVF measured on the cross-sectioned B3 sample. Raman spectra collected along (e) the center, and (f) the outer layer of the column. The three curves in each graph represent triplicates. (g) Map of mPVF capturing one edge and center of a column in the section as represented by the black box in (a). Scale bar indicates 8m. [27].

4.2.2 Chemical Degradation tracked through Monoclinic Phase Volume Fraction

The measured monoclinic phase was previously quantified in work by Barrett et al., [27], finding its concentrations throughout the 3D probed volume through a monoclinic phase volume fraction (mPVF) equation, eq. 4.1, which was created from a model established by Clarke and Adar [75]. This equation uses the intensity values of the 182 and 191 cm^{-1} monoclinic peaks and the intensity values of the 148 and 263 cm^{-1} tetragonal peaks. The

$$mPVF(\%) = \frac{I_m^{182} + I_m^{191}}{0.97 * (I_t^{148} + I_t^{263}) + (I_m^{182} + I_m^{182})} \tag{4.1}$$

The tetragonal phase volume fraction (tPVF) was also calculated as a validation, shown in eq. 4.2, from an equation established by Perry et al. [76].

$$tPVF(\%) = \frac{I_t^{263}}{(I_t^{263} + I_m^{182})} \tag{4.2}$$

The corresponding intensity of the bands mentioned for the Raman shifts in eq. 4.1 and eq. 4.2 were fitted using a pseudo-Voigt function using MATLAB and its nonlinear least squares solver for curve fitting. Then using the equations, the 3D volumes as well as the box and whisker plots, shown in Fig. 4.2 where created. For the box and whisker plots in Fig. 4.2(c,f), the plot is used to indicate the maximum and minimum mPVF values as well as the standard deviation and average mPVF value for each depth measurement and should not be confused as to indicate outliers within the data.

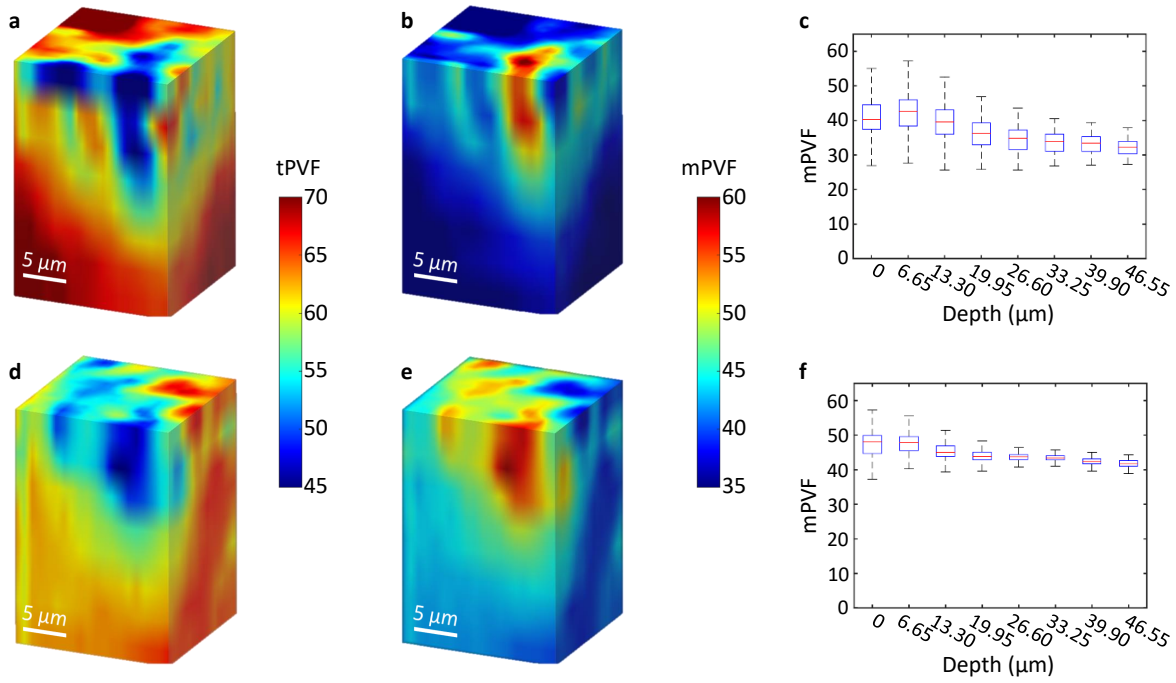

Figure 4.2: 3D reconstruction of (a) tetragonal and (b) monoclinic phase volume fractions of B2 sample (1250°C, 1 h annealed), (c) variation of mPVF along the depth in B2 (d) tetragonal and (e) monoclinic phase volume fractions of B3 sample (1250°C, 10 h annealed), and (f) variation of mPVF along the depth B3 sample [27].

The main results of these findings were that a majority of the thermochemical degradation, quantified through the formation of the monoclinic phase, occurs within the first hour of CMAS infiltration. This also implies that the thermochemical degradation greatly aggravates the thermo-mechanical degradation of the coating within the first hour too. Only around a 10% increase in the mPVF is observed from the 1 h sample to the 10 h sample at the surface. Locally, it was observed that the phase transformation was higher in areas directly exposed to CMAS and had a higher surface area of contact, the edges of the columns, as compared to the center of the columns.

CHAPTER 5
OUTCOMES OF RESIDUAL STRESS MEASUREMENTS OF CMAS-INFILTRATED THERMAL BARRIER COATINGS

Contents within this chapter have been published in:

Z. Stein,R. Naraparaju, U. Schulz, L. Tetard, and S. Raghavan, "Residual stress effects of CMAS infiltration in high temperature jet engine ceramic coatings captured non-destructively with confocal Raman-based 3D rendering." *Journal of the European Ceramic Society*, 2022. doi: 10.1016/j.jeurceramsoc.2022.11.003 [20]

The residual stress and its evolution within CMAS-exposed thermal barrier coatings were investigated through confocal Raman spectroscopy. The residual stress state of the coating demonstrated predominantly thermomechanical components, such as coating stiffening and sintering, contributing towards the overall residual stress state of the coating after 1h of infiltration with minor contribution from thermochemical components, relating to coating phase destabilization and the formation of a monoclinic phase from the ZrO_2 polymorph. Conversely, the thermochemical components became more prominent in its contribution towards the overall residual stress state of the coating after 10h of infiltration as compared to the aforementioned thermomechanical components. Discussions of these results, their implications, and the relationship between phase

destabilization and the residual stress state of the coating are further expanded upon within the sections of this chapter.

5.1 Data Fitting and Processing of the Raman spectroscopy peaks

Previous literature has found the tetragonal peak labeled at 643.78 cm^{-1} is stress sensitive and an excellent candidate for quantifying the stress within tetragonal ZrO_2. The unstressed reference of the tetragonal 643.78 cm^{-1} peak used within this study is based on a full freestanding EB-PVD 4 mol% YSZ coating from Tanaka et al. [63]. From this unstressed reference peak position, any shifts could be attributed to additional stresses introduced to the coating as a result of CMAS infiltration. A shift to a lower relative wavenumber corresponds to a chemical bond associated with the tetragonal peak in the coating that is experiencing tension (also known as a red shift). Likewise, if the measured peak shifts to higher relative wavenumber, then the coating is experiencing compression (also known as a blue shift). An experimentally determined piezo-spectroscopic coefficient associated with the 643.78 cm^{-1} peak can then be used to quantify the stress the coating is experiencing [62]. Similar to tracking degradation through the phase concentration [27, 77], using this Raman shift and piezo-spectroscopic coefficient stress relationship equation, eq. 5.1 allows for the tracking and quantification of the stress evolution throughout CMAS-induced degradated coating. It is from quantifying the stress in multiple 2D Raman hyperspectral maps at increasing depths in the coating that a 3D reconstruction can be created to track the residual stress evolution of the coating as a result of CMAS degradation throughout a probed volume.

$$\Delta\sigma \approx \frac{\nu - \nu_0}{\Pi} \tag{5.1}$$

Fig. 5.1 shows a collection of nine peaks relating to the tetragonal and monoclinic peaks that will be considered in this thesis. This collection of peaks are organized by their rough location as well as the phases of these peaks as either t-phase or m-phase for the tetragonal and monoclinic phases, respectively. The peaks locations observed previously in literature as well as their respective piezo-spectroscopic coefficient (Π), if measured, are listed for each respective peak [62, 78, 79, 80, 81, 82]. The Raman spectra peaks that will primarily be considered for stress analysis consist of two sets of doublet peaks, [62, 80, 81, 82], associated with both the tetragonal peaks, 607.1 cm^{-1} [77] and 643.78 cm^{-1} [63], as well as the monoclinic peaks, 615.2 cm^{-1} [77] and 637.6 cm^{-1} [77]. Another tetragonal peak located at 463.7cm^{-1}, [50, 62], and a monoclinic doublet at 479.49 and 507.88 cm^{-1}, [79], were used to compare the trends of stress. These peak positions are indicated as vertical dashed lines in Fig. 5.3. Since these four peaks are so close together and influence each other when convoluted, these four peaks must be deconvoluted before the residual stress results can be determined and discussed.

Peak	Raman Shift (cm^{-1})	[1] Observed Pk. Π Coeff.	[2] Observed Pk. Π Coeff.	[3] Observed Pk. Π Coeff.	[4] Observed Pk. Π Coeff.	[5] Observed Pk. Π Coeff.	[6] Observed Pk. Π Coeff.	Peak ID (t/mYSZ)
1	180 cm^{-1}	180 cm^{-1}	178.29 cm^{-1}	N/A	180 cm^{-1}	177 cm^{-1}	180 cm^{-1}	mYSZ
2	190 cm^{-1}	192 cm^{-1}	189.38 cm^{-1}	N/A	192 cm^{-1}	189 cm^{-1}	192 cm^{-1}	mYSZ
3	460 cm^{-1}	473 cm^{-1}	461.72 cm^{-1}	461.6 cm^{-1} 5.58 $cm^{-1}GPa^{-1}$	N/A	466 cm^{-1}	N/A	tYSZ
4	476 cm^{-1}	476 cm^{-1}	479.49 cm^{-1}	N/A	477 cm^{-1}	474 cm^{-1}	476 cm^{-1}	mYSZ
5	502 cm^{-1}	502 cm^{-1}	507.88 cm^{-1}	N/A	N/A	500 cm^{-1}	503 cm^{-1}	mYSZ
6	610 cm^{-1}	615 cm^{-1}	604.76 cm^{-1}	N/A	N/A	N/A cm^{-1}	N/A	tYSZ
7	615 cm^{-1}	617 cm^{-1}	622.18 cm^{-1}	N/A	619 cm^{-1}	615 cm^{-1}	616 cm^{-1}	mYSZ
8	637 cm^{-1}	638 cm^{-1}	647.23 cm^{-1}	N/A	638 cm^{-1}	638 cm^{-1}	638 cm^{-1}	mYSZ
9	640 cm^{-1}	640 cm^{-1}	641.21 cm^{-1}	648.5 cm^{-1} 2.79 $cm^{-1}GPa^{-1}$	N/A	637 cm^{-1}	N/A	tYSZ

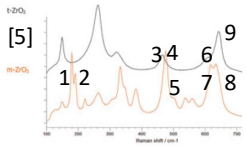

KEY:
[1] Phillippi & Mazdiyasni (1971)
[2] Pezzotti & Porporati (2004)
[3] Bouvier & Lucazeau (2000)
[4] Arunkumar & Babu (2018)
[5] Kypraiou & Eliades (2012)
[6] Kim & Hamaguchi (1997) [Includes additional 6 references in a table]

Figure 5.1: A collection of nine peaks for the tetragonal (t-phase), denoted by green, and monoclinic (m-phase) peaks, denoted by pink, used within this thesis as well as previously reported observed peak locations and piezo-spectroscopic coefficients, if measured, for these nine peaks.

It is worth bearing in mind moving forward that Raman spectroscopy is unable to directly and easily distinguish between the peaks within the yttria-rich stabilized tetragonal-prime phase and the similar yttria-lean transformable tetragonal phase, so the peaks associated with both have been labelled as the tetragonal phase throughout this thesis paper. These four peaks were deconvoluted using a nonlinear least squares solver within MATLAB and were fitted using a pseudo-Voigt function. The monoclinic phase volume fraction (mPVF) values found in a previous investigation reported in [27] and relative peak relationships including the intensity ratios and full width at half

maximum peak values were used as additional initial parameter values for defining the pseudo-Voigt function to both improve the overall fittings and their consistency between points. Fig. 5.2 illustrates the influence of inclusion of the mPVF fitting parameter.

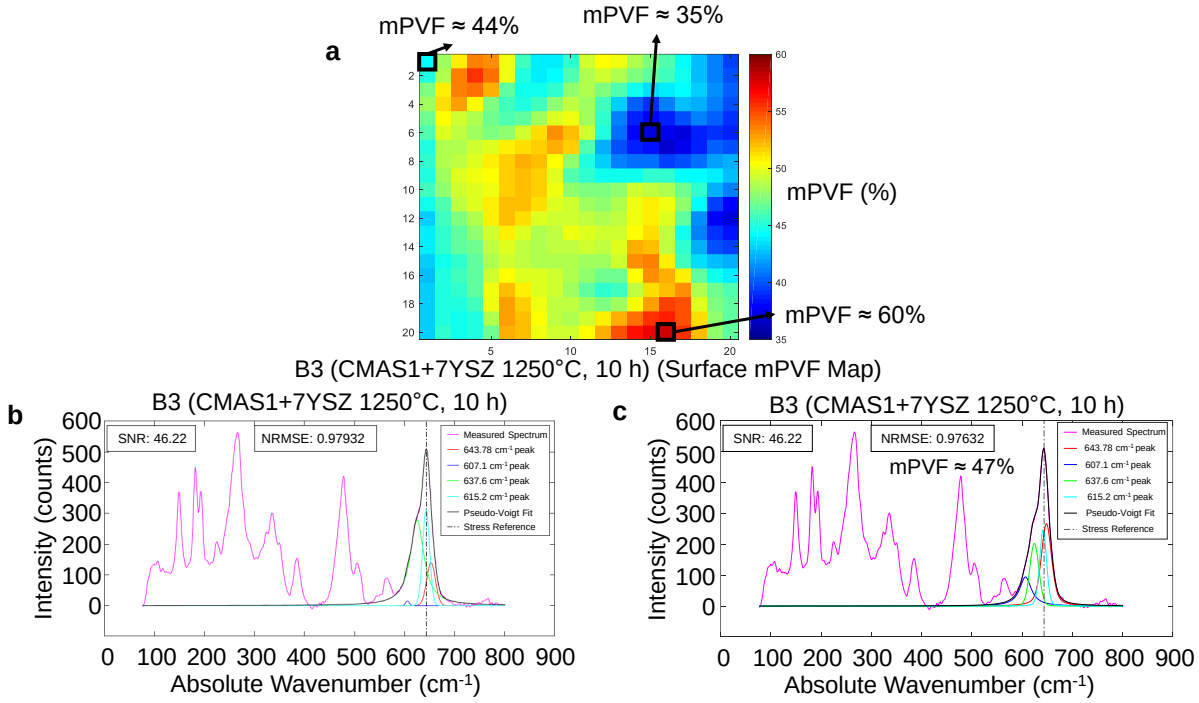

Figure 5.2: (a) The mPVF map for B3 (CMAS1+7YSZ 1250°C, 10 h) at the surface, [27]. The pseudo-Voigt fitting deconvolution (b) without and (c) with considering the mPVF for each point. The signal-to-noise ratio and the normalized root mean square equation goodness of fit are shown as SNR and NRMSE, respectively.

For points where there is a smaller influence of the monoclinic phase on the spectra (lower mPVF), this fitting parameter did not change much. However, in regions where there are higher mPVF, and therefore higher influence of the monoclinic doublet in the convolution of peaks, this

fitting parameter had a much more significant impact on the fittings. To keep consistency, this mPVF fitting parameter was used for each point throughout each map through the depth of the coating. An example of the final results of this deconvolution for both the monoclinic and tetragonal doublets as well as the residual, signal-to-noise ratio, and normalized root mean square equation (NRMSE) goodness of fit equation where 1.0 is a perfect fit is shown in Fig. 5.3.

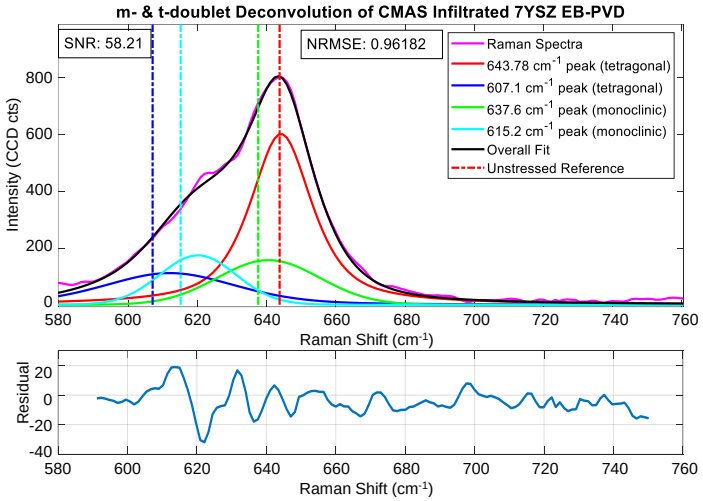

Figure 5.3: The deconvolution of the monoclinic (m) and tetragonal (t) doublets around the 643.78 cm^{-1} peak. Additional measurement and goodness of fit parameters are also shown through the signal-to-noise ratio and the normalized root mean square equation goodness of fit, shown as SNR and NRMSE, respectively. The residual differences between the fitted and measured peaks are plotted in the lower graph.

The stress reference peak position reference and the piezo-spectroscopic coefficient reported by Tanaka et al. is used for the 643.78 cm^{-1} tetragonal ZrO_2 Raman band since their measurements were conducted on a similar free standing 7YSZ EB-PVD coating [63]. This allows for the changes in the residual stress solely due to the coating's interaction with CMAS to be more

accurately quantified when coupled with the PS-coefficient. This stress reference peak position takes into account the stresses induced to the ZrO_2 bonds when structured through EB-PVD spray as compared to ZrO_2 nano-powder.

Additionally, it should be noted that there is are two broad cubic peak spanning throughout the 500 - 650 cm^{-1} Raman shift range with one of the cubic peaks having a maximum around 617^{-1} [83]. Due to its very broad nature, it was found that fitting this peak had little influence on the resulting peak locations of the remaining tetragonal and monoclinic doublets, and therefore was found to be negligible and are not considered in the fitting results.

A 2D stress map for each depth was obtained by applying eq. 5.1 to each deconvoluted 643.78 cm^{-1} peak in every point of the 2D map. These 2D maps were then stacked by their respective probed depths creating a 3D reconstruction of the probed volume. This reconstruction was performed for each sample by compiling and importing the sequence of 2D maps into the volume viewer plugin with a trilinear interpolation within ImageJ.

5.2 Stress Results for CMAS-infiltrated TBCs with respect to Annealing Time

Using the stress calculation method detailed in 5.1, volumetric reconstructions of the Raman stress are considered for non-infiltrated sample A3, annealed at 1250°C for 10 h (Fig. 5.4(a)), and for CMAS infiltrated samples B2 and B3, annealed at 1250°C for 1 h and 10 h Fig. 5.4(b,c), as well as the average stresses throughout the depth of the probed volume Fig. (5.4(d)). The non-infiltrated A3 sample serves as a stress reference of the 7YSZ EB-PVD coating prior to infiltration

and can therefore be compared to the CMAS infiltrated samples. The extent that CMAS influences the stress state of the coating over an increased exposure and annealing time can be extracted from using the non-infiltrated sample as the reference point since this will minimize the influence the coating-substrate interface has on the coating's residual stress. The non-infiltrated sample also serves as a reference to evaluate the CMAS infiltrated B3 sample, both of which have been annealed at the same temperature and duration.

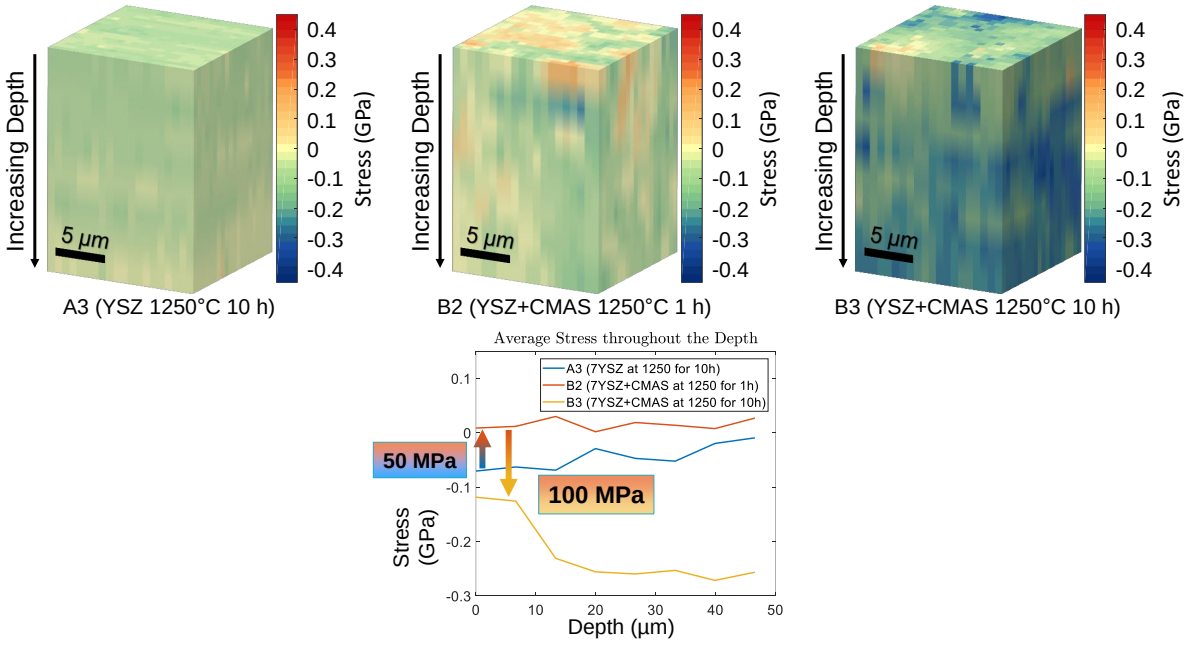

Figure 5.4: 3D reconstruction of the stress for the 643.78 cm^{-1} peak for (a) a non-infiltrated 7YSZ sample annealed at 1250°C for 10 h (A3), (b) a CMAS infiltrated 7YSZ sample annealed at 1250°C for 1 h (B2), and (c) a CMAS infiltrated 7YSZ sample annealed at 1250°C for 10 h. (d) Average stress as a function of depth for A3, B2 and B3.

It can be observed that the non-infiltrated sample has a very uniform stress state after being annealed for 10 h at 1250°C (Fig. 5.4(a)). Compression estimated at 100 MPa was calculated throughout the volume of the coat. This compression within the probed volume of the coating is typical for columnar microstructures of EB-PVD coatings [6]. As a non-infiltrated EB-PVD coating ages, the gradient of compressive stress coming from the growth of the thermally grown oxide layer at the interface is expected to increase as the thermal grown oxide layer becomes more developed early in a coating system's lifetime, causing the coating to experience more compression [6].

CMAS exposure and its infiltration is observed to have an effect on the stress state of the coating in Fig. 5.4(b-d). After 1 h of infiltration, the overall average stress state of the coating becomes slightly tensile, as observed in the red line in Fig. 5.4(d). The tensile loading is likely a result of both the coating stiffening from CMAS infiltrating the intercolumnar gaps of the coating as well as coating sintering [52]. Additionally, non-uniform stresses appear in the probed volume of the coating in Fig. 5.4(b). While some regions still display a similar stress state to that of the non-infiltrated sample, other regions are experiencing around 100 MPa of tension. This variation can be attributed to the local microstructure of the coating. While molten, CMAS infiltrates throughout the intercolumnar gaps and feather arms of the EB-PVD columns and then solidifies before stiffening the coating upon cooling [19, 43, 84]. As a result, there are higher concentrations of CMAS within these intercolumnar gaps. This is not only observed with higher monoclinic concentrations as in [27], but also within the residual stresses of the coating. While other factors will influence

the overall residual stress state within the microstructure, there will be a trend towards a red shift, tension, for the edges of the 7YSZ columns as well as any coating surfaces in contact with CMAS.

After 10 h of infiltration, as seen in Fig. 5.4(c), the overall stress state of the coating drastically changes, shifting to an average state of compression. While there still are small regions of tension, as observed after 1 h of infiltration, a majority of the coating is ranging from around 100 MPa of compression at the surface to around 300 MPa of compression around 46 μm into the depth of the coating, noted in the yellow line in Fig. 5.4(d). As compared to the non-infiltrated sample, which was also annealed for 10 h at 1250°C, the average stress state of the coating overall is also more compressive on and around the edges of the columns. This higher stress state of compression as well as the minor shift from tension to compression in most regions can be attributed to phase destabilization and subsequent phase transformation of the coating. Additionally, this trend towards of a residual stress profile first becoming more tensile and then transforming to become more compressive with increased CMAS exposure and annealing times aligns with what has been found in literature [50, 85, 86].

Yttria is used in YSZ to stabilize ZrO_2 into the tetragonal state, referred to as tetragonal-prime. Over time, molten CMAS leaches enough yttria from the coating to transform from the tetragonal phase into cubic and monoclinic phases [22, 32, 40, 50, 53]. The phase transformation from tetragonal to monoclinic has been associated with a volumetric expansion of the lattice structure of approximately 3 - 5%, while little change within the lattice structure from a tetragonal to cubic phase transformation is expected [19, 21, 23, 25, 30, 50, 52, 56, 57, 87, 88]. However, this thermochemical mechanism of phase destabilization and transformation is delayed and much slower

acting than the thermomechanical effects of CMAS infiltration through CMAS-induced coating stiffening [22, 26].

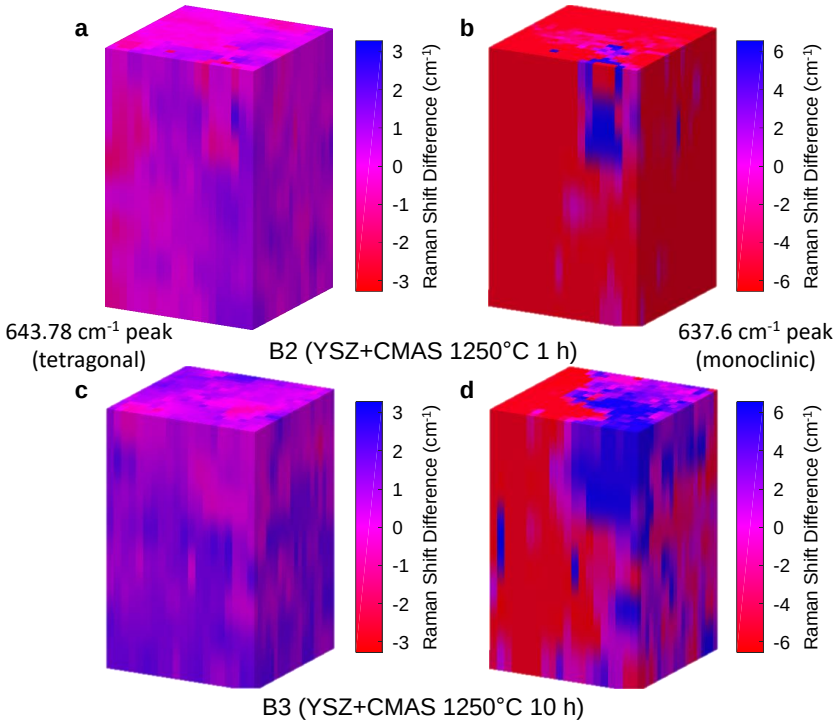

Figure 5.5: 3D reconstruction based on Raman shifts of the 643.78 and 637.6 cm^{-1}, tetragonal and monoclinic peaks, respectively, for CMAS infiltrated 7YSZ samples annealed at 1250°C for (a) 1 h and (b) 10 h. Shifts are relative to the unstressed peak position references in [63, 77].

Volumetric reconstructions of the Raman stress-induced peak shifts are shown in Fig. 5.5 for both the 643.78 cm^{-1} tetragonal peak of B2 and B3 coatings, Fig. 5.5(a,c) respectively, and for 637.6 cm^{-1} monoclinic peak of B2 and B3 coatings, Fig. 5.5(b,d) respectively. These peak shifts can be quantified into stress using the piezo-spectroscopic coefficients and the Raman shift and piezo-spectroscopic relationship equation, eq. 5.1. In both cases, the higher the wavenumber is from the unstressed peak reference of the tetragonal 643.78 cm^{-1} [63] and monoclinic 637.6 cm^{-1}

[77] peaks, blue shift, is indicative of compression. Conversely, the lower the wavenumber from the unstressed peak references, red shift, is indicative of tension.

It can be observed that after 1 h of annealing that, overall, the tetragonal peak has red shifted towards tension as well as the monoclinic peak. Then after 10 h of annealing, the tetragonal peak has shifted more to a blue shift in compression. The monoclinic peak for 10 h of annealing, while split, has more of a compressive blue shift, similar to the tetragonal peak at 10 h, but has also retained its tensile red shift in some areas. The red and blue shifts in the monoclinic peak corresponds to both microstructure as well as the presence and concentration of the monoclinic phase in those regions. Areas with a lower presence of the monoclinic phase will naturally have a weaker Raman signal than regions with higher monoclinic concentrations.

In addition to the 643.78 cm^{-1} tetragonal peak, the 463.7 cm^{-1} peak has also been used previously in literature to measure the stress of the non-transformable tetragonal phase [50, 62]. The 463.7 cm^{-1} peak was used as a form of validation of the results within this study. For this validation the unstressed reference peak position is 463.7 cm^{-1} [50, 62] and the piezo-spectroscopic coefficient used is 5.6 cm^{-1} GPa^{-1} [62]. It should be noted that this coefficient is for air plasma sprayed 5YSZ, meaning some minor discrepancy will be present as compared to what the coefficient would be for the 463.7 cm^{-1} peak for EB-PVD 7YSZ. Similarly, a 488 nm Ar/Kr laser was reported in Krämer et al. [50], compared to the 532 nm He/Ne laser used within this study. The stress for the 463.7 cm^{-1} peak is reported in Fig. 5.6. A similar trend in the localized stress distribution between the intercolumnar gaps and on and at the edge of the columns to what was found in Fig. 5.4 is observed. However, there are differences within the overall average stress states

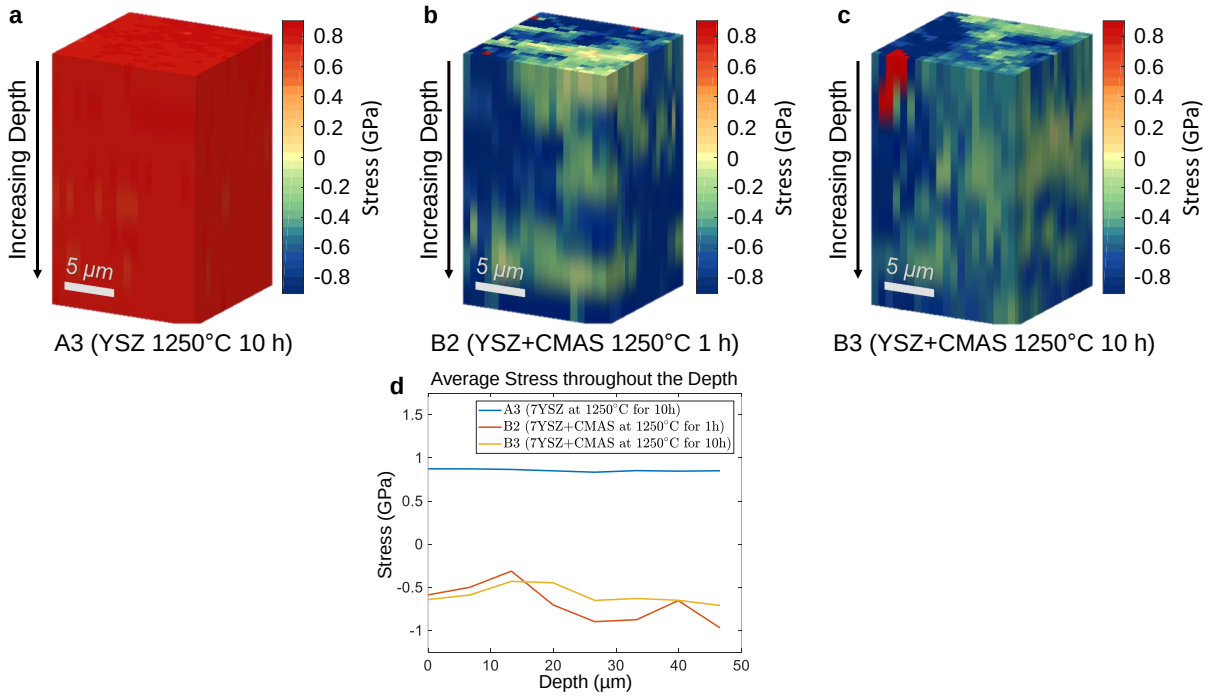

Figure 5.6: 3D reconstruction of the stress for the 463.7 cm^{-1} peak for (a) a non-infiltrated 7YSZ sample annealed at 1250°C for 10 h (A3), (b) a CMAS infiltrated 7YSZ sample annealed at 1250°C for 1 h (B2), and (c) a CMAS infiltrated 7YSZ sample annealed at 1250°C for 10 h (B3) as well as (d) the average stress as a function of depth for all three samples.

throughout the depth. Most notably, the overall reported stress state within the non-infiltrated sample (Fig. 5.6(a)), while uniform, is estimated at nearly 1 GPa in tension. While high, using the residual stress within the non-infiltrated sample as a reference for the infiltrated, it is observed that both the infiltrated samples are more in compression relative to the non-infiltrated sample. The localized microstructural effects on the stress distribution also influence the stress state of the probed volume. The intercolumnar gaps tend to be less compressive than on or at the edge of the columns.

A schematic of the stress evolution of the coating as a result of CMAS infiltration summarizing our observations is shown in Fig. 5.7. Fig. 5.7(a) is a schematic of the pristine columnar microstructure prior to CMAS infiltration. The columnar tips are well defined and feather arms can be observed along the edges of these columnar finger-like structures. The center of these columns would be in compression and a stress gradient to a less stressed or more neutral state is present approaching the edge of these columns. As molten CMAS deposits onto the surface of the coating, as seen in Fig. 5.7(b), it infiltrates to some depth as seen in Fig. 5.7(c). Distinct stress regions form, which can be distinguished between the infiltrated and non-infiltrated zones of the coating. These differences in the stress state of the coating within these two zones matches the literature [50]. The depth at which the CMAS infiltrates is dependent on the operating temperatures as well as infiltration time. With the thermal gradient present from the surface of the coating to the interface of the coating, bond coat, and substrate, commonly the CMAS will infiltrate to a certain depth and solidify as it reaches below melting temperatures within the coating. This infiltration can also be interrupted if the operating temperatures of the turbine decreases. Depending on the temperature, the CMAS might not solidify, resulting in full infiltration of the entire thickness of

the coating. At the beginning of CMAS exposure, the effects of infiltration depth on the residual stress of the coating is immediately observable [89].

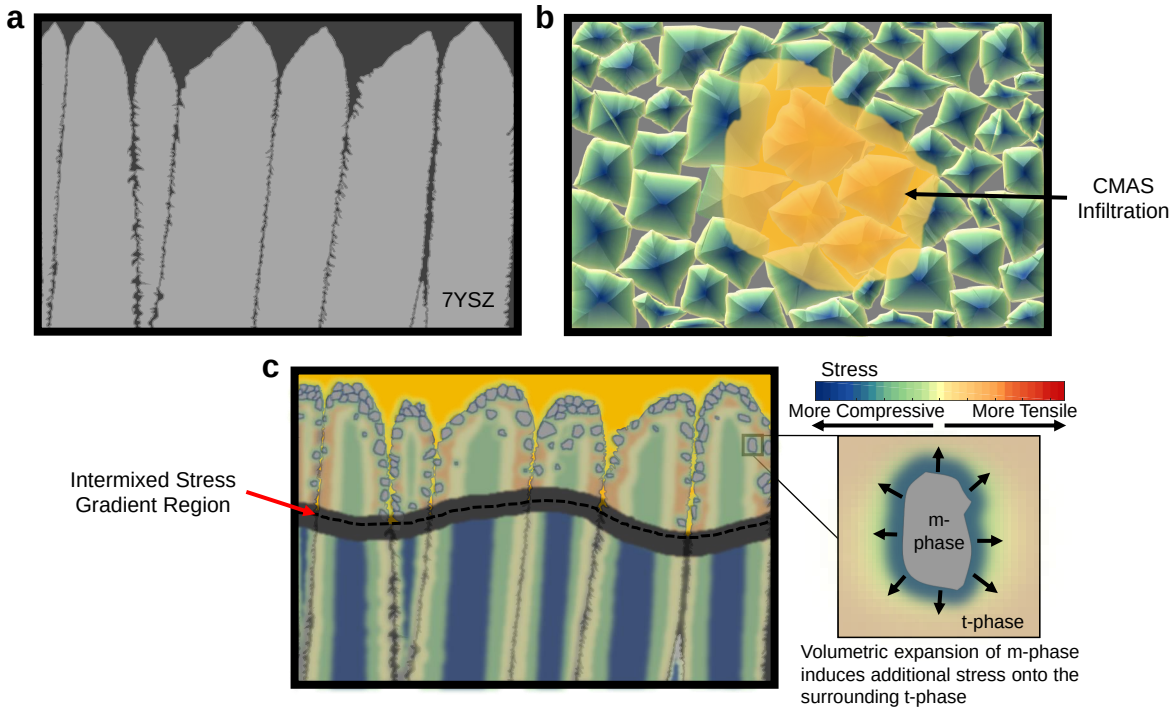

Figure 5.7: Schematics of (a) a pristine 7YSZ EB-PVD coating cross-section prior to any CMAS exposure or infiltration. (b) Top down view of the 7YSZ EB-PVD coating, showing cut-aways of the columns as well as a region for CMAS infiltration. (c) The cross-section of the 7YSZ EB-PVD coating after some time that CMAS as infiltrated and interacted with the coating, allowing for substantial monoclinic formation to occur.

Primarily two different types of stresses are introduced during infiltration. The first is purely mechanical and the second is purely chemical. The mechanical stress comes as the coating sinters as well as stiffens when the CMAS solidifies within an infiltrated region and displays a tensile stress state similar to that observed during aging with the bulk splat-like microstructure of air

plasma sprayed coatings [69, 90]. In this case, the solidified CMAS would start to pull the columns of the coating in tension and cause a stress gradient from the edge of these columns to the column center. This stress is also fast acting, occurring immediately upon CMAS solidification and will be the predominant stress contributor early in the coating's exposure to CMAS. Depending on the extent and intensity of this additional residual stress, the coating may already start to fail through the formation, propagation, and coalescence of cracks [26]. The chemically induced stress occurs over longer periods of exposure and over several cycles of temperature fluctuations. Phase destabilization leading to phase transformation occurs upon cooling below approximately 600°C within the yttria-lean parts of the 7YSZ. This leads to the transformation of the tetragonal phase to the monoclinic phase [31]. As observed in a previous investigation in this work [27], a majority of this phase transformation into the monoclinic phase occurs by 1 h of CMAS exposure and infiltration and only slightly increases by 10 h. Though it should also be noted that the concentration and extent of this phase transformation becomes more developed throughout measured probed volume of the coating over time. The newly transformed monoclinic phase induces a compressive force onto the surrounding coating due to its volumetric expansion during phase transformation. Since this stress is dependent on the concentration and on the rate of monoclinic phase volume fraction growth, this stress is slow acting and becomes more dominant over longer exposure times. In high enough concentrations, this chemically-induced stress would negate the aforementioned mechanically-induced tensile stress and push the coating into a residual stress profile of compression.

Outside of this infiltrated region, the coating would behave as it did prior to CMAS deposition. However, as represented in Fig. 5.7(c), an interface between the infiltrated and non-infiltrated regions would result in some mismatch between the residual stress states. This intermixed stress region would introduce a gradient between the two stress states of the infiltrated and non-infiltrated and would depend on additional parameters, such as, but not limited to, the infiltration depth and the age of the coating. It is at this interface zone that cracks and CMAS-related spallation are be most likely to occur, especially when considering the accumulation of stresses at the interface [91], coefficient of thermal expansion mismatch, and thermal loading during an operational cycle.

The monoclinic phase volume fraction (mPVF), as previously described in [27], and its relationship to stress can be observed in Fig. 5.8. For Fig. 5.8(a,b), mPVF and stress stack maps throughout the depth of the coating are shown for both CMAS-infiltrated samples for 1 h of annealing, Fig. 5.8(a), and 10 h of annealing, Fig. 5.8(b). Within both of these stack maps are highlighted regions displaying relatively low and high mPVF concentrations for each sample. All mPVF and stress measurements within the low and high mPVF regions were then averaged throughout the depth and are summarized in Fig. 5.8(c,d). For the CMAS infiltrated sample annealed at 1250°C for 1 h, Fig. 5.8(a,c), it can be observed that regions with low mPVF are more in tension as compared to region with high mPVF, which are more in compression. This can be observed in the average stress and mPVF throughout the depth plots for the low and high mPVF regions. On average, the stress in the low mPVF region is around 50 MPa in tension. The mPVF varies between 20 - 30% in this low mPVF region. The stress being in tension follows what has been observed in literature for CMAS exposed coatings with little phase transformation [22, 52]. Meanwhile, the

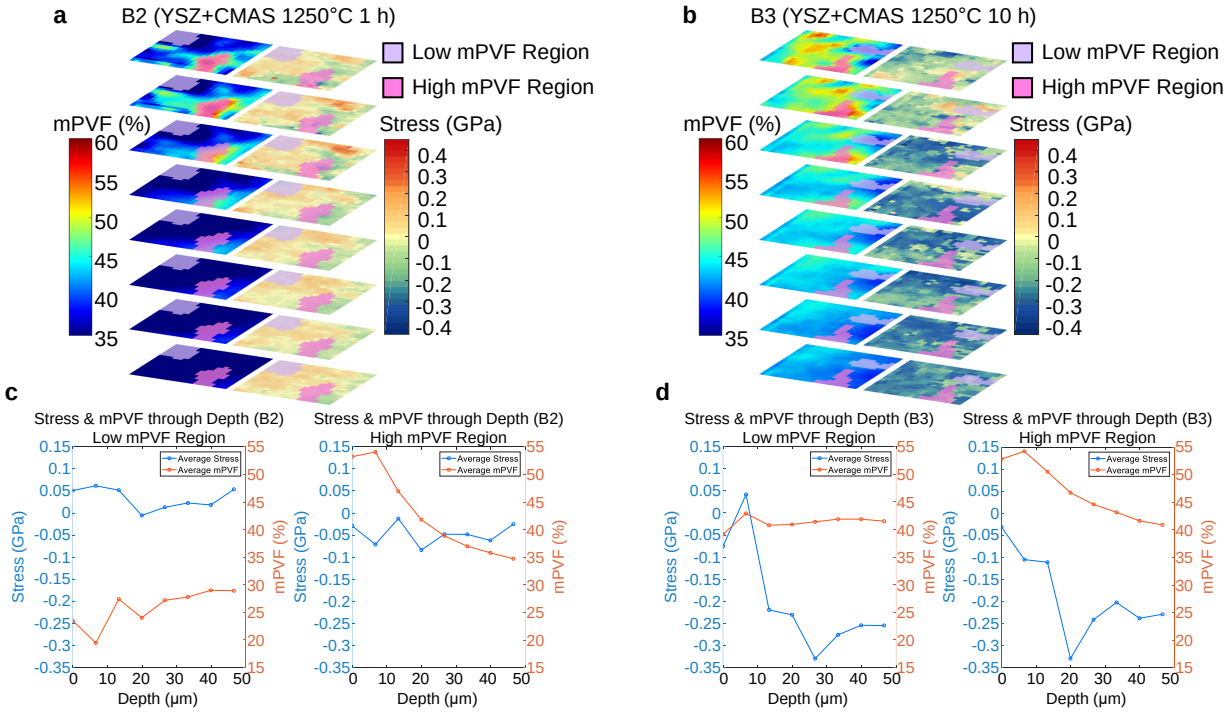

Figure 5.8: A comparison of the localized monoclinic phase concentrations, measured through the phase volume fraction (mPVF) [27], and the localized stress state of the probed areas throughout the probed depth of the coating are shown for samples infiltrated by CMAS annealed at 1250°C for (a) 1 h and (b) 10 h. For both samples, relatively low and high mPVF regions were selected and mPVF and stress were tracked within these regions throughout the depth of the coating for the (c) 1 h and (d) 10 h samples.

stress in the high mPVF region is around 50 MPa in compression. The mPVF in this high region starts around 55% and decreases towards around 35% around 46 μm into the depth of the coating.

As the monoclinic phase becomes more developed throughout the coating after annealing a CMAS infiltrated sample at 1250°C for 10 h, Fig. 5.8(b,d), the stress does not vary as drastically between low and high mPVF regions relative to the sample. Both regions have an average stress starting around 50 MPa in compression at the surface and becomes more compressive throughout the depth of the coating until reaching around 250 MPa in compression around 46 μm into the depth of the coating. The low mPVF region is relatively consistent throughout the depth of the coating with a mPVF at around 40%. The high mPVF region starts around 55% and decreases to around 40% around 46 μm into the depth of the coating.

Comparing the 1 h and 10 h annealing samples, it can be observed that there is some threshold range of mPVF, in which the residual stress state of the coating is dependent on. Below this threshold, the additional residual stresses introduced by CMAS infiltration are dominated primarily by physical mechanisms, such as coating stiffening. Above this threshold, the additional stresses introduced are dominated more by chemical mechanisms, such as the phase transformation of the coating. Finally, as the mPVF approaches this threshold, the stress state of the coating would slowly shift from tension to compression, as what is seen between the low and high mPVF regions for the 1 h annealed sample in Fig. 5.8(c). This trend has also been noted in literature [50, 85]. It is noted that additional exposure studies with a more comprehensive annealing time sample matrix between 1 h and 10 h would be needed to better quantify this transitional point and to observe how this value may change due to varying coating conditions and ageing. From the results in Fig.

5.8(c,d), the transition from tension to compression appears around a mPVF of 35% for EB-PVD 7YSZ coatings exposed to CMAS early in its lifetime. This is observed in the 1 h annealed sample where the residual stress shifts from being in tension for the low mPVF region to compression for the high mPVF region. This shift into compression is continued when comparing the high mPVF region of the 1 h annealed sample, Fig. 5.8(c) with the low mPVF region of the 10 h annealed sample, Fig. 5.8(d). An increase in the mPVF, when comparing the low mPVF region and the high mPVF region of the 10 h annealed sample, has minimal effects on the residual stresses of the coating beyond an mPVF of 40%.

5.3 Correlation and Relationship between mPVF and Stress and its implications

A linear Karl Pearson Correlation Coefficient calculation, eq. 5.2, was performed to establish a correlation relationship between the mPVF and stress at varying monoclinic concentrations, where R is the correlation coefficient, n is the sample size, mPVF is the concentration of mPVF at a given point, and σ is the stress calculated at a given point. The resulting correlation coefficients calculated can be seen in Table 5.1. Eq. 5.2 is the linear Karl Pearson Correlation Coefficient equation and this equation provides a linear coefficient value between -1 to 1, where -1 would indicate a purely negative linear relationship in which there is an inversely proportional relationship trend between the mPVF and stress. Conversely, 1 would indicate a purely positive linear relationship in which there is a proportional relationship trend between the mPVF and stress. Another important value would be 0, which would indicate no linear relationship between the mPVF and stress values.

$$R = \frac{n\Sigma(mPVF\,\sigma) - (\Sigma mPVF)(\Sigma\sigma)}{\sqrt{[n\Sigma(mPVF^2) - (\Sigma mPVF)^2][n\Sigma(\sigma^2) - (\Sigma\sigma)^2]}} \tag{5.2}$$

Due to the varying mechanisms influencing stress, such as the mPVF concentration as observed in Fig. 5.8, all probed points on the surface measurement were put into one of three different sections: a low mPVF, medium mPVF, and high mPVF region. The range for each of these regions were determined relatively for each CMAS infiltrated sample by equally distributing the three ranges between the minimum mPVF value and the maximum mPVF value previously calculated. Since there is an uneven distribution of the mPVF values across the samples, the sample size is not consistent among the different regions and has been taken into consideration in the standard error calculations, eq. 5.3.

$$SE_R = \sqrt{\frac{1 - R^2}{n - 2}} \tag{5.3}$$

Strong correlations can be observed for both CMAS infiltrated samples across the low, medium, and high mPVF sections. This is expected since previous literature has established phase transformations having the ability to influence the overall stress state of the coating [28, 89]. The low mPVF section for B2 (1250°C, 1 h) has the lowest correlation coefficient, relative to the other coefficients and mPVF sections. This is explained by the chemical mechanisms influencing stress being weakest within the low mPVF section while the physical mechanisms being more dominant with a mPVF lower than the transitional point around 35% mentioned previously when

Table 5.1: Pearson correlation coefficients between the calculated mPVF and stress, categorized by low mPVF, medium mPVF, and high mPVF ranges relative to the CMAS infiltrated 7YSZ samples annealed at 1250°C for (B2) 1 h and (B3) 10 h.

Sample	Low mPVF (0 - 20.2)	Medium mPVF (20.2 - 40.4)	High mPVF (40.4 - 60.5)
B2 (7YSZ+CMAS, 1250°C for 1 h)	0.62 $\pm$ 0.08	0.97 $\pm$ 0.01	-0.93 $\pm$ 0.04

Sample	Low mPVF (36.8 - 43.9)	Medium mPVF (43.9 - 50.9)	High mPVF (50.9 - 58.0)
B3 (7YSZ+CMAS, 1250°C for 10 h)	-0.91 $\pm$ 0.05	-0.95 $\pm$ 0.03	-0.90 $\pm$ 0.06

comparing the mPVF and stress evolution throughout the depth in Fig. 5.8. The correlation coefficient value then increases through the transition from the physically dominant to chemically dominant mechanisms for the residual stress as the monoclinic concentration increases and the residual stress becomes compressive within the medium mPVF and high mPVF sections. The high mPVF section for the 1 h sample as well as all of the mPVF sections for the 10 h sample have a negative coefficient due to the notation of tensile stresses being "postive" and compressive stresses being "negative" in stress calculations. The 10 h sample, B3, as a relatively uniform correlation coefficient with little deviation across the low, medium, and high mPVF sections. This suggests that the transition to chemically dominated mechanisms, which impacts the overall residual stress

profile of the coating the most, has already been completed.

CHAPTER 6
CONCLUSIONS

This final chapter provides a summary of the conclusions highlighting the overall impacts as well as the contributions both within these findings as well as overall towards the broader scientific community. This chapter will conclude with the progression of future work and the plans moving forward as a result of the conclusions within this thesis.

6.1 Conclusions

In this study, the localized residual stress within CMAS-infiltrated EB-PVD YSZ samples were observed to experience two different mechanisms using 3D confocal Raman spectroscopy with microscale resolution. The first relates to thermomechanical mechanisms, such as coating stiffening and CMAS closing the intercolumnar gaps of EB-PVD, almost immediately inducing tensile stresses on the residual stress state of the coating. The second relates to thermochemical mechanisms, such as coating dissolution into the CMAS melt and phase transformation, and is slower acting. The compressive stress induced onto the coating results from monoclinic phase formation and increases as the concentration of the monoclinic phase increases over time. For low-cycled 7YSZ EB-PVD coatings exposed to CMAS, a monoclinic phase volume fraction of about 35% was found

to be the point at which thermochemical mechanisms become the dominate stress mechanism as compared to thermomechanical mechanisms below this threshold value. After 1 h of infiltration, the residual stress state of the coating, as measured by tetragonal phase, at the surface shifted 50 MPa in tension relative to the non-infiltrated coating. Then after 10 h of infiltration, the residual stress shifted 100 MPa in compression relative to the 1 h infiltrated coating.

Key Outcomes:

- Thermomechanical mechanisms, such as coating stiffening, influences the coating residual stress state almost immediately and shifted the coating, on average, in a state of tension.
- Thermochemical mechanisms, such as phase transformations, occurs much more slowly for 7YSZ coatings in influencing the coating residual stress state. Over time, the coating shifted to a state of compression as the monoclinic phase volume fractions (mPVF) increased over annealing time.
- For 7YSZ EB-PVD coatings with little aging exposed to CMAS, an mPVF of around 35% was observed to be the point in which the thermochemical mechanisms provided enough of a compressive stress to counteract the thermomechanical mechanisms providing tensile stress.
- After 1 h of infiltration, the tetragonal coating stress was 100 MPa in tension, redshift.
- After 10 h of infiltration, tetragonal coating stress shifted 100 MPa in compression, blueshift.
- The thermomechanical and thermochemical mechanisms have a non-linear influence on the residual stress state of the coating as CMAS infiltrates over time.

- The edges and surfaces of the EB-PVD columns were observed to be more sensitive to the residual stress effects from CMAS infiltration than regions with lower exposure to CMAS, such as the columnar cores and centers.

The results from this thesis aids in the elucidation of the infiltration micro-mechanisms influencing the residual stress of the CMAS-exposed coatings in a microscale spatial resolution. Understanding and being able to quantify how CMAS infiltration over time influences the the residual stress as well as the development of these mechanisms, thermomechanical and thermochemical, and their contributions to the overall residual stress of the coating is essential when considering potential CMAS mitigation strategies and when developing novel more CMAS-resistant and more durable coatings.

6.2 Future Work

Minimizing CMAS infiltration or minimizing its effects on the high temperature ceramic coating is essential towards mitigating the effects of CMAS on coatings. As can be observed in this thesis, thermomechanical mechanisms occur much more rapidly than thermochemical mechanisms currently for 7YSZ coatings. Using coating compositions, such as gadolinium zirconate ($Gd_2Zr_2O_7$ (GZO)), where the coating reacts so rapidly with the CMAS melt that it forms an apatite and garnet reactionary layer that inhibits further CMAS infiltration into the depth of the coating may be beneficial in limiting the overall effects of CMAS [50, 51, 92, 93]. Utilizing GZO-like rapid reactionary responses in coatings for other compositions may reduce the overall degradation impact

of CMAS. The formation of these reactionary products can be tracked in-situ non-destructively through 3D confocal Raman Spectroscopy. Some limitations regarding Raman measurements at high temperatures will need to be considered and mitigated, such as peak broadening that occurs at elevated temperatures [31]. Improvements are also needed to be made regarding the measurement collection times to achieve higher temporal resolutions to capture in-situ the intermediary interactions occurring during infiltration. Similarly as these reactionary products are forming and being tracked, the residual stress can also be captured and changes in these stresses can be observed as CMAS comes into contact with the coating and as the coating interacts and reacts to the CMAS melt itself. 3D confocal Raman Spectroscopy can also be used for other novel coating systems such as environmental barrier coatings (EBCs) since this method is not limited only to 7YSZ or thermal barrier coatings. A better understanding on the limitations of this method is needed to capture the capabilities of EBCs and other traditionally air-plasma sprayed coatings.

APPENDIX A
COPYRIGHT PERMISSION

Author rights

The below table explains the rights that authors have when they publish with Elsevier, for authors who choose to publish either open access or subscription. These apply to the corresponding author and all co-authors.

Author rights in Elsevier's proprietary journals	**Published open access**	**Published subscription**
Retain patent and trademark rights	√	√
Retain the rights to use their research data freely without any restriction	√	√
Receive proper attribution and credit for their published work	√	√
Re-use their own material in new works without permission or payment (with full acknowledgement of the original article): 1. Extend an article to book length 2. Include an article in a subsequent compilation of their own work 3. Re-use portions, excerpts, and their own figures or tables in other works.	√	√
Use and share their works for scholarly purposes (with full acknowledgement of the original article): 1. In their own classroom teaching. Electronic and physical distribution of copies is permitted 2. If an author is speaking at a conference, they can present the article and distribute copies to the attendees 3. Distribute the article, including by email, to their students and to research colleagues who they know for their personal use 4. Share and publicize the article via Share Links, which offers 50 days' free access for anyone, without signup or registration 5. Include in a thesis or dissertation (provided this is not published commercially) 6. Share copies of their article privately as part of an invitation-only work group on commercial sites with which the publisher has a hosting agreement	√	√
Publicly share the preprint on any website or repository at any time.	√	√
Publicly share the accepted manuscript on non-commercial sites	√	√ using a CC BY-NC-ND license and usually only after an embargo period (see Sharing Policy for more information)
Publicly share the final published article	√ in line with the author's choice of end user license	×
Retain copyright	√	×

APPENDIX B
COPYRIGHT PERMISSION

Institution rights

Regardless of how the author chooses to publish with Elsevier, their institution has the right to use articles for classroom teaching and internal training. Articles can be used for these purposes throughout the author's institution, not just by the author:

Institution rights in Elsevier's proprietary journals (providing full acknowledgement of the original article is given)	**All articles**
Copies can be distributed electronically as well as in physical form for classroom teaching and internal training purposes	√
Material can be included in coursework and courseware programs for use within the institution (but not in Massive Open Online Courses)	√
Articles can be included in applications for grant funding	√
Theses and dissertations which contain embedded final published articles as part of the formal submission can be posted publicly by the awarding institution with DOI links back to the formal publication on ScienceDirect	√

LIST OF REFERENCES

[1] R. A. Miller, "Current status of thermal barrier coatings—an overview," *Surface and Coatings Technology*, vol. 30, no. 1, pp. 1–11, 1987.

[2] ——, "Thermal barrier coatings for aircraft engines: history and directions," *Journal of thermal spray technology*, vol. 6, no. 1, pp. 35–42, 1997.

[3] A. G. Evans, D. Mumm, J. Hutchinson, G. Meier, and F. Pettit, "Mechanisms controlling the durability of thermal barrier coatings," *Prog. Mater. Sci.*, vol. 46, no. 5, pp. 505–553, 2001.

[4] N. P. Padture, M. Gell, and E. H. Jordan, "Thermal barrier coatings for gas-turbine engine applications," *Science*, vol. 296, no. 5566, pp. 280–284, 2002.

[5] K. Knipe, A. Manero II, S. F. Siddiqui, C. Meid, J. Wischek, J. Okasinski, J. Almer, A. M. Karlsson, M. Bartsch, and S. Raghavan, "Inside the engine environment–synchrotrons reveal secrets of high-temperature ceramic coatings," *Am. Ceram. Soc. Bull.*, vol. 94, no. 1, p. 22, 2015.

[6] Y. Sohn, K. Vaidyanathan, M. Ronski, E. Jordan, and M. Gell, "Thermal cycling of eb-pvd/mcraly thermal barrier coatings: Ii. evolution of photo-stimulated luminescence," *Surf. Coat. Technol.*, vol. 146, pp. 102–109, 2001.

[7] H. Worch, "P. kofstad, high temperature corrosion. elsevier applied science, london/new york 1988, 546 seiten mit 222 illustr. und 6 tabellen,£ 68.00, isbn 1-85166-154-9," 1989.

[8] D. Clarke and C. Levi, "Materials design for the next generation thermal barrier coatings," *Annual review of materials research*, vol. 33, no. 1, pp. 383–417, 2003.

[9] I. Sumner and D. Ruckle, "Development of improved-durability plasma sprayed ceramic coatings for gas turbine engines," in *16th Joint Propulsion Conference*, 1980, p. 1193.

[10] T. J. Carter, "Common failures in gas turbine blades," *Engineering Failure Analysis*, vol. 12, no. 2, pp. 237–247, 2005.

[11] M. Murugan, A. Ghoshal, M. Walock, L. G. Bravo, R. Koneru, N. Jain, C. Mock, M. Pepi, A. Nieto, A. Flatau *et al.*, "In search of durable sandphobic thermal/environmental barrier coatings for rotorcraft gas turbine engines," in *AIAA Scitech 2021 Forum*, 2021, p. 0874.

[12] B. J. Connolly, E. Loth, and C. F. Smith, "Efficiency of inertial particle separators," *Powder Technology*, p. 118004, 2022.

[13] M. S. Hammer, A. van Donkelaar, C. Li, A. Lyapustin, A. M. Sayer, N. C. Hsu, R. C. Levy, M. J. Garay, O. V. Kalashnikova, R. A. Kahn *et al.*, "Global estimates and long-term trends of fine particulate matter concentrations (1998–2018)," *Environmental Science & Technology*, vol. 54, no. 13, pp. 7879–7890, 2020.

[14] A. R. Ericks, F. W. Zok, D. L. Poerschke, and C. G. Levi, "Protocol for selecting exemplary silicate deposit compositions for evaluating thermal and environmental barrier coatings," *Journal of the American Ceramic Society*, vol. 105, no. 6, pp. 3665–3688, 2022.

[15] R. Wellman and J. Nicholls, "Erosion, corrosion and erosion–corrosion of eb pvd thermal barrier coatings," *Tribology International*, vol. 41, no. 7, pp. 657–662, 2008.

[16] L. Steinberg, R. Naraparaju, M. Heckert, C. Mikulla, U. Schulz, and C. Leyens, "Erosion behavior of eb-pvd 7ysz coatings under corrosion/erosion regime: Effect of tbc microstructure and the cmas chemistry," *Journal of the European Ceramic Society*, vol. 38, no. 15, pp. 5101–5112, 2018.

[17] X. Zhang, X. Shan, P. J. Withers, X. Zhao, and P. Xiao, "Tracking the calcium-magnesium-alumino-silicate (cmas) infiltration into an air-plasma spray thermal barrier coating using x-ray imaging," *Scripta Materialia*, vol. 176, pp. 94–98, 2020.

[18] X. Shan, D. Wu, H. Cai, L. Luo, L. Yang, L. Jia, F. Guo, and X. Zhao, "Cmas attack behavior of air plasma sprayed thermal barrier coatings with big pores," *Journal of the European Ceramic Society*, 2022.

[19] R. Naraparaju, M. Hüttermann, U. Schulz, and P. Mechnich, "Tailoring the eb-pvd columnar microstructure to mitigate the infiltration of cmas in 7ysz thermal barrier coatings," *J. Eur. Ceram. Soc.*, vol. 37, no. 1, pp. 261–270, 2017.

[20] Z. Stein, R. Naraparaju, U. Schulz, L. Tetard, and S. Raghavan, "Residual stress effects of cmas infiltration in high temperature jet engine ceramic coatings captured non-destructively

with confocal raman-based 3d rendering," *Journal of the European Ceramic Society*, 2022. [Online]. Available: https://www.sciencedirect.com/science/article/pii/S0955221922008640

[21] M. P. Borom, C. A. Johnson, and L. A. Peluso, "Role of environment deposits and operating surface temperature in spallation of air plasma sprayed thermal barrier coatings," *Surf. Coat. Technol.*, vol. 86, pp. 116–126, 1996.

[22] S. Krämer, J. Yang, C. G. Levi, and C. A. Johnson, "Thermochemical interaction of thermal barrier coatings with molten cao–mgo–al2o3–sio2 (cmas) deposits," *J. Am. Ceram. Soc.*, vol. 89, no. 10, pp. 3167–3175, 2006.

[23] J. Wu, H.-b. Guo, Y.-z. Gao, and S.-k. Gong, "Microstructure and thermo-physical properties of yttria stabilized zirconia coatings with cmas deposits," *J. Eur. Ceram. Soc.*, vol. 31, no. 10, pp. 1881–1888, 2011.

[24] H. Chang, C. Cai, Y. Wang, Y. Zhou, L. Yang, and G. Zhou, "Calcium-rich cmas corrosion induced microstructure development of thermal barrier coatings," *Surf. Coat. Technol.*, vol. 324, pp. 577–584, 2017.

[25] C. Mercer, S. Faulhaber, A. Evans, and R. Darolia, "A delamination mechanism for thermal barrier coatings subject to calcium–magnesium–alumino-silicate (cmas) infiltration," *Acta Mater.*, vol. 53, no. 4, pp. 1029–1039, 2005.

[26] L. Li, N. Hitchman, and J. Knapp, "Failure of thermal barrier coatings subjected to cmas attack," *J. Therm. Spray Technol.*, vol. 19, no. 1, pp. 148–155, 2010.

[27] C. Barrett, Z. Stein, J. Hernandez, R. Naraparaju, U. Schulz, L. Tetard, and S. Raghavan, "Detrimental effects of sand ingression in jet engine ceramic coatings captured with raman-based 3d rendering," *J. Eur. Ceram. Soc.*, vol. 41, no. 2, pp. 1664–1671, 2021.

[28] U. Schulz, "Phase transformation in eb-pvd yttria partially stabilized zirconia thermal barrier coatings during annealing," *J. Am. Ceram. Soc.*, vol. 83, no. 4, pp. 904–910, 2000.

[29] C. Viazzi, J.-P. Bonino, and F. Ansart, "Synthesis by sol-gel route and characterization of yttria stabilized zirconia coatings for thermal barrier applications," *Surf. Coat. Technol.*, vol. 201, no. 7, pp. 3889–3893, 2006.

[30] R. Naraparaju, U. Schulz, P. Mechnich, P. Döbber, and F. Seidel, "Degradation study of 7 wt.% yttria stabilised zirconia (7ysz) thermal barrier coatings on aero-engine combustion chamber parts due to infiltration by different cao–mgo–al2o3–sio2 variants," *Surf. Coat. Technol.*, vol. 260, pp. 73–81, 2014.

[31] H. F. Garces, B. S. Senturk, and N. P. Padture, "In situ raman spectroscopy studies of high-temperature degradation of thermal barrier coatings by molten silicate deposits," *Scr. Mater.*, vol. 76, pp. 29–32, 2014.

[32] R. Wellman, G. Whitman, and J. Nicholls, "Cmas corrosion of eb pvd tbcs: Identifying the minimum level to initiate damage," *Int. J. Refract. Hard Met.*, vol. 28, no. 1, pp. 124–132, 2010.

[33] Q. Ahmed, I. N. Qureshi, and I. U. Salam, "Investigation of hot section (nozzle guiding vane) distress due to interaction of thermal barrier coatings with cmas," in *Key Engineering Materials*, vol. 778. Trans Tech Publ, 2018, pp. 245–250.

[34] B. Liu, Y. Liu, C. Zhu, H. Xiang, H. Chen, L. Sun, Y. Gao, and Y. Zhou, "Advances on strategies for searching for next generation thermal barrier coating materials," *Journal of Materials Science & Technology*, vol. 35, no. 5, pp. 833–851, 2019.

[35] L. Shi, Z. Sun, and Y. Lu, "The combined influences of film cooling and thermal barrier coatings on the cooling performances of a film and internal cooled vane," *Coatings*, vol. 10, no. 9, p. 861, 2020.

[36] I. Spitsberg and K. More, "Effect of thermally grown oxide (tgo) microstructure on the durability of tbcs with ptnial diffusion bond coats," *Materials Science and Engineering: A*, vol. 417, no. 1-2, pp. 322–333, 2006.

[37] W. A. Nelson and R. M. Orenstein, "Tbc experience in land-based gas turbines," *J. Therm. Spray Technol.*, vol. 6, no. 2, pp. 176–180, 1997.

[38] U. Schulz, S. Terry, and C. Levi, "Microstructure and texture of eb-pvd tbcs grown under different rotation modes," *Mater. Sci. Eng. A*, vol. 360, no. 1-2, pp. 319–329, 2003.

[39] J. L. Smialek, "The chemistry of saudi arabian sand: a deposition problem on helicopter turbine airfoils," in *Gordon Conference on Corrosion*, no. NAS 1.15: 105234, 1991.

[40] C. G. Levi, J. W. Hutchinson, M.-H. Vidal-Sétif, and C. A. Johnson, "Environmental degradation of thermal-barrier coatings by molten deposits," *MRS Bull.*, vol. 37, no. 10, pp. 932–941, 2012.

[41] P. Mechnich and W. Braue, "Solid-state cmas corrosion of an eb-pvd ysz coated turbine blade: Zr4+ partitioning and phase evolution," *J. Am. Ceram. Soc.*, vol. 98, no. 1, pp. 296–302, 2015.

[42] R. Naraparaju, J. J. G. Chavez, P. Niemeyer, K.-U. Hess, W. Song, D. B. Dingwell, S. Lokachari, C. Ramana, and U. Schulz, "Estimation of cmas infiltration depth in eb-pvd tbcs: A new constraint model supported with experimental approach," *Journal of the European Ceramic Society*, vol. 39, no. 9, pp. 2936–2945, 2019.

[43] M. R. Kabir, A. K. Sirigiri, R. Naraparaju, and U. Schulz, "Flow kinetics of molten silicates through thermal barrier coating: A numerical study," *Coatings*, vol. 9, no. 5, p. 332, 2019.

[44] F. Stott, R. Taylor, and D. De Wet, "The effects of molten silicate deposits on the stability of thermal barrier coatings for turbine applications at very high temperatures," in *Proceedings of advanced materials*, 1992.

[45] R. W. Bruce, "Development of 1232 c (2250 f) erosion and impact tests for thermal barrier coatings," *Tribology transactions*, vol. 41, no. 4, pp. 399–410, 1998.

[46] J. Nicholls, M. Deakin, and D. Rickerby, "A comparison between the erosion behaviour of thermal spray and electron beam physical vapour deposition thermal barrier coatings," *Wear*, vol. 233, pp. 352–361, 1999.

[47] A. G. Evans, D. R. Clarke, and C. G. Levi, "The influence of oxides on the performance of advanced gas turbines," *Journal of the European Ceramic Society*, vol. 28, no. 7, pp. 1405–1419, 2008.

[48] X. Montero, R. Naraparaju, M. Galetz, and U. Schulz, "Study of cmas infiltration and evaporation behaviour under water vapour/sulphur oxide conditions in eb-pvd 7ysz," *Corrosion Science*, vol. 198, p. 110123, 2022.

[49] T. R. Kakuda, C. G. Levi, and T. D. Bennett, "The thermal behavior of cmas-infiltrated thermal barrier coatings," *Surf. Coat. Technol.*, vol. 272, pp. 350–356, 2015.

[50] S. Krämer, S. Faulhaber, M. Chambers, D. R. Clarke, C. G. Levi, J. W. Hutchinson, and A. Evans, "Mechanisms of cracking and delamination within thick thermal barrier systems in aero-engines subject to calcium-magnesium-alumino-silicate (cmas) penetration," *Mater. Sci. Eng. A*, vol. 490, no. 1-2, pp. 26–35, 2008.

[51] J. J. G. Chavez, R. Naraparaju, C. Mikulla, P. Mechnich, K. Kelm, C. Ramana, and U. Schulz, "Comparative study of eb-pvd gadolinium-zirconate and yttria-rich zirconia coatings performance against fe-containing calcium-magnesium-aluminosilicate (cmas) infiltration," *Corrosion Science*, vol. 190, p. 109660, 2021.

[52] H. Peng, L. Wang, L. Guo, W. Miao, H. Guo, and S. Gong, "Degradation of eb-pvd thermal barrier coatings caused by cmas deposits," *Prog. Nat. Sci.: Mater. Int*, vol. 22, no. 5, pp. 461–467, 2012.

[53] G. Pujol, F. Ansart, J.-P. Bonino, A. Malié, and S. Hamadi, "Step-by-step investigation of degradation mechanisms induced by cmas attack on ysz materials for tbc applications," *Surf. Coat. Technol.*, vol. 237, pp. 71–78, 2013.

[54] M. A. Rivera-Gil, J. J. Gomez-Chavez, C. Ramana, R. Naraparaju, U. Schulz, and J. Muñoz-Saldaña, "High temperature interaction of volcanic ashes with 7ysz tbc's produced by aps: Infiltration behavior and phase stability," *Surface and Coatings Technology*, vol. 378, p. 124915, 2019.

[55] J. J. G. Chavez, R. Naraparaju, P. Mechnich, K. Kelm, U. Schulz, and C. Ramana, "Effects of yttria content on the cmas infiltration resistance of yttria stabilized thermal barrier coatings system," *Journal of Materials Science & Technology*, vol. 43, pp. 74–83, 2020.

[56] D. M. Lipkin, J. A. Krogstad, Y. Gao, C. A. Johnson, W. A. Nelson, and C. G. Levi, "Phase evolution upon aging of air-plasma sprayed t-zirconia coatings: I—synchrotron x-ray diffraction," *J. Am. Ceram. Soc.*, vol. 96, no. 1, pp. 290–298, 2013.

[57] M. Ishigame and T. Sakurai, "Temperature dependence of the raman spectra of zro2," *J. Am. Ceram. Soc.*, vol. 60, no. 7-8, pp. 367–369, 1977.

[58] R. Naraparaju, U. Schulz, S. Raghavan, and E. Bohorquez, "Non-destructive cmas-infiltration characterization of thermal barrier coatings," Nov. 17 2020, uS Patent 10,837,918.

[59] ——, "Zerstörungsfreie cmas-infiltrationscharakterisierung von wärmesperrbeschichtungen," September 2019.

[60] Y. C. Cho and S. I. Ahn, "Fabricating a raman spectrometer using an optical pickup unit and pulsed power," *Scientific reports*, vol. 10, no. 1, pp. 1–8, 2020.

[61] C. V. Raman and K. S. Krishnan, "A new type of secondary radiation," *Nature*, vol. 121, no. 3048, pp. 501–502, 1928.

[62] P. Bouvier and G. Lucazeau, "Raman spectra and vibrational analysis of nanometric tetragonal zirconia under high pressure," *J. Phys. Chem. Solids*, vol. 61, no. 4, pp. 569–578, 2000.

[63] M. Tanaka, R. Kitazawa, T. Tomimatsu, Y. Liu, and Y. Kagawa, "Residual stress measurement of an eb-pvd y2o3-zro2 thermal barrier coating by micro-raman spectroscopy," *Surf. Coat. Technol.*, vol. 204, no. 5, pp. 657–660, 2009.

[64] L. He, X. Zhou, B. Zhong, Z. Xu, R. Mu, G. Huang, and X. Cao, "Phase evolution, interdiffusion and failure of la2 (zr0. 7ce0. 3) 2o7/ysz thermal barrier coatings prepared by electron beam–physical vapor deposition," *Journal of Alloys and Compounds*, vol. 624, pp. 137–147, 2015.

[65] Z. Shen, L. He, Z. Xu, R. Mu, and G. Huang, "Morphological evolution and failure of lzc/ysz dcl tbcs by electron beam-physical vapor deposition," *Materialia*, vol. 4, pp. 340–347, 2018.

[66] A. M. Limarga, J. Iveland, M. Gentleman, D. M. Lipkin, and D. R. Clarke, "The use of larson–miller parameters to monitor the evolution of raman lines of tetragonal zirconia with high temperature aging," *Acta materialia*, vol. 59, no. 3, pp. 1162–1167, 2011.

[67] T. R. Kakuda, A. M. Limarga, T. D. Bennett, and D. R. Clarke, "Evolution of thermal properties of eb-pvd 7ysz thermal barrier coatings with thermal cycling," *Acta Materialia*, vol. 57, no. 8, pp. 2583–2591, 2009.

[68] C. Mercer, J. Williams, D. Clarke, and A. Evans, "On a ferroelastic mechanism governing the toughness of metastable tetragonal-prime (t) yttria-stabilized zirconia," *Proceedings of the Royal Society A: Mathematical, Physical and Engineering Sciences*, vol. 463, no. 2081, pp. 1393–1408, 2007.

[69] A. M. Limarga, R. Vaßen, and D. R. Clarke, "Stress distributions in plasma-sprayed thermal barrier coatings under thermal cycling in a temperature gradient," *Journal of Applied Mechanics*, vol. 78, no. 1, 2011.

[70] C. Cai, S. Chang, Y. Zhou, L. Yang, G. Zhou, and Y. Wang, "Microstructure characteristics of eb-pvd ysz thermal barrier coatings corroded by molten volcanic ash," *Surface and Coatings Technology*, vol. 286, pp. 49–56, 2016.

[71] A. R. Krause, H. F. Garces, G. Dwivedi, A. L. Ortiz, S. Sampath, and N. P. Padture, "Calcia-magnesia-alumino-silicate (cmas)-induced degradation and failure of air plasma sprayed yttria-stabilized zirconia thermal barrier coatings," *Acta Mater.*, vol. 105, pp. 355–366, 2016.

[72] F. Foucher, "Influence of laser shape on thermal increase during micro-raman spectroscopy analyses," *Journal of Raman Spectroscopy*, vol. 53, no. 3, pp. 664–676, 2022.

[73] D. Tuschel, "Selecting an excitation wavelength for raman spectroscopy," *Spectroscopy*, vol. 31, no. 3, pp. 14–23, 2016.

[74] L. Li and D. R. Clarke, "Effect of cmas infiltration on radiative transport through an eb-pvd thermal barrier coating," *International journal of applied ceramic technology*, vol. 5, no. 3, pp. 278–288, 2008.

[75] D. Clarke and F. Adar, "Measurement of the crystallographically transformed zone produced by fracture in ceramics containing tetragonal zirconia," *Journal of the American Ceramic Society*, vol. 65, no. 6, pp. 284–288, 1982.

[76] C. Perry, D.-W. Liu, and R. P. INGEL, "Phase characterization of partially stabilized zirconia by raman spectroscopy," *Journal of the american ceramic society*, vol. 68, no. 8, pp. C–184, 1985.

[77] P. Barberis, T. Merle-Méjean, and P. Quintard, "On raman spectroscopy of zirconium oxide films," *J. Nucl. Mater.*, vol. 246, no. 2-3, pp. 232–243, 1997.

[78] C. Phillippi and K. Mazdiyasni, "Infrared and raman spectra of zirconia polymorphs," *Journal of the American Ceramic Society*, vol. 54, no. 5, pp. 254–258, 1971.

[79] G. Pezzotti and A. A. Porporati, "Raman spectroscopic analysis of phase-transformation and stress patterns in zirconia hip joints," *Journal of biomedical optics*, vol. 9, no. 2, pp. 372–384, 2004.

[80] P. Arunkumar, U. Aarthi, M. Sribalaji, B. Mukherjee, A. K. Keshri, W. H. Tanveer, S.-W. Cha, and K. S. Babu, "Deposition rate dependent phase/mechanical property evolution in zirconia and ceria-zirconia thin film by eb-pvd technique," *J. Alloys Compd.*, vol. 765, pp. 418–427, 2018.

[81] V. Kypraiou, S. Pelekanos, and G. Eliades, "Identification of monoclinic phase in cad/cam zirconia fpd frameworks," *Eur. J. Esthet. Dent.*, vol. 7, no. 4, pp. 418–429, 2012.

[82] B.-K. Kim and H.-o. Hamaguchi, "Mode assignments of the raman spectrum of monoclinic zirconia by isotopic exchange technique," *Phys. Status Solidi B*, vol. 203, no. 2, pp. 557–563, 1997.

[83] D. Gazzoli, G. Mattei, and M. Valigi, "Raman and x-ray investigations of the incorporation of ca2+ and cd2+ in the zro2 structure," *Journal of Raman Spectroscopy: An International Journal for Original Work in all Aspects of Raman Spectroscopy, Including Higher Order Processes, and also Brillouin and Rayleigh Scattering*, vol. 38, no. 7, pp. 824–831, 2007.

[84] M. Vidal-Setif, N. Chellah, C. Rio, C. Sanchez, and O. Lavigne, "Calcium–magnesium–alumino-silicate (cmas) degradation of eb-pvd thermal barrier coatings: Characterization of cmas damage on ex-service high pressure blade tbcs," *Surf. Coat. Technol.*, vol. 208, pp. 39–45, 2012.

[85] G. Pezzotti, K. Yamada, S. Sakakura, and R. P. Pitto, "Raman spectroscopic analysis of advanced ceramic composite for hip prosthesis," *J. Am. Ceram. Soc.*, vol. 91, no. 4, pp. 1199–1206, 2008.

[86] P. Yáñez-Contreras, M. León-Rodríguez, J. M. Medina-Flores, J. A. Jiménez-García, F. J. Santander-Bastida, and J. Yáñez-Rodríguez, "Determination of residual stresses in thermal barrier coating due to the amount of cmas infiltration," *Dyna*, vol. 87, no. 215, pp. 76–83, 2020.

[87] A. Mirgorodsky, M. Smirnov, and P. Quintard, "Phonon spectra evolution and soft-mode instabilities of zirconia during the c–t–m transformation," *J. Phys. Chem. Solids*, vol. 60, no. 7, pp. 985–992, 1999.

[88] C. M. Ramos, A. S. Tabata, P. F. Cesar, J. H. Rubo, P. A. S. Fracisconi, and A. F. S. Borges, "Application of micro-raman spectroscopy to the study of yttria-stabilized tetragonal zirconia polycrystal (y-tzp) phase transformation," *Appl. Spectrosc.*, vol. 69, no. 7, pp. 810–814, 2015.

[89] C. Chiu, S. Tseng, C. Chao, X. Fan, and W. Cheng, "Interfacial stresses of thermal barrier coating with film cooling holes induced by cmas infiltration," *Coatings*, vol. 12, no. 3, p. 326, 2022.

[90] H. Dong, G.-J. Yang, C.-X. Li, X.-T. Luo, and C.-J. Li, "Effect of tgo thickness on thermal cyclic lifetime and failure mode of plasma-sprayed tbc s," *J. Am. Ceram. Soc.*, vol. 97, no. 4, pp. 1226–1232, 2014.

[91] G. Xu, L. Yang, and Y. Zhou, "A coupled theory for deformation and phase transformation due to cmas infiltration and corrosion of thermal barrier coatings," *Corros. Sci.*, vol. 190, p. 109690, 2021.

[92] U. Schulz, R. Naraparaju, L. Hochstein, and B. Kanka, "Lifetime evaluation of various new eb-pvd and aps tbcs in thermal in thermal gradient and fct," 2018.

[93] L. Steinberg, C. Mikulla, R. Naraparaju, P. Pavlov, M. Löffler, U. Schulz, and C. Leyens, "Erosion behavior of cmas/va infiltrated eb-pvd gd2zr2o7 tbcs: Special emphasis on the effect of mechanical properties of the reaction products," *Wear*, vol. 506, p. 204450, 2022.